Bio-Design and Manufacturing (2025) 8:461–481
https://doi.org/10.1631/bdm.2400280

RESEARCH ARTICLE

Innovative dual-physical bioreactor for quantifying the synergistic effects of electro-stiffness coupling stimulation on cancer cells

Qunfeng Yang[1,2] · **Qing Zhang**[1]

Received: 17 July 2024 / Accepted: 7 November 2024

Abstract

Cells live in a multiphysics-coupled microenvironment in vivo, in which electric fields (EFs) and mechanical cues are the most essential induction signals. The regulatory effects of EFs and stiffness on cells have been independently demonstrated. However, how cells respond to electromechanical coupling cues remains mysterious. In this study, an electro-stiffness-coupled chip system was designed and fabricated, freely integrating and precisely controlling EF strength and the mechanical stiffness applied to cells across the physiological spectrum. Utilizing the innovative bioreactor, it was observed that electromechanical coupling stimulations can shape cancer cell morphology and cytoskeleton into a unique anteroposterior polarization state and orient cancer cell migration in a voltage-dependent manner through cytoskeleton-associated mechanisms. Moreover, the mechanical stiffness regulated cancer cell susceptibility to EFs, and the orientation effect of EFs on cells required a stiffness threshold. Furthermore, transforming growth factor-β1 suppressed the orientation of cancer cells induced by electromechanical coupling signals and showed a splitting effect on the directionality and velocity of cancer cell migration, indicating a comprehensive cross-talk of biochemical–electromechanical signals. Together with the dual-physical bioreactor we designed, these findings provide a robust and convenient platform for exploring cellular responses to electro-stiffness coupling signals, reveal the biophysical mechanisms of cell polarization and migration from the perspective of electromechanical coupling, and lay a promising foundation for biophysical-based cell manipulation and therapeutic interventions.

✉ Qing Zhang
zhangqing@bjast.ac.cn

[1] Institute of New Materials and Advanced Manufacturing, Beijing Academy of Science and Technology, Beijing 100089, China

[2] School of Pharmacy and Laboratory Medicine, Guangdong Chaozhou Health Vocational College, Chaozhou 521000, China

Graphical abstract

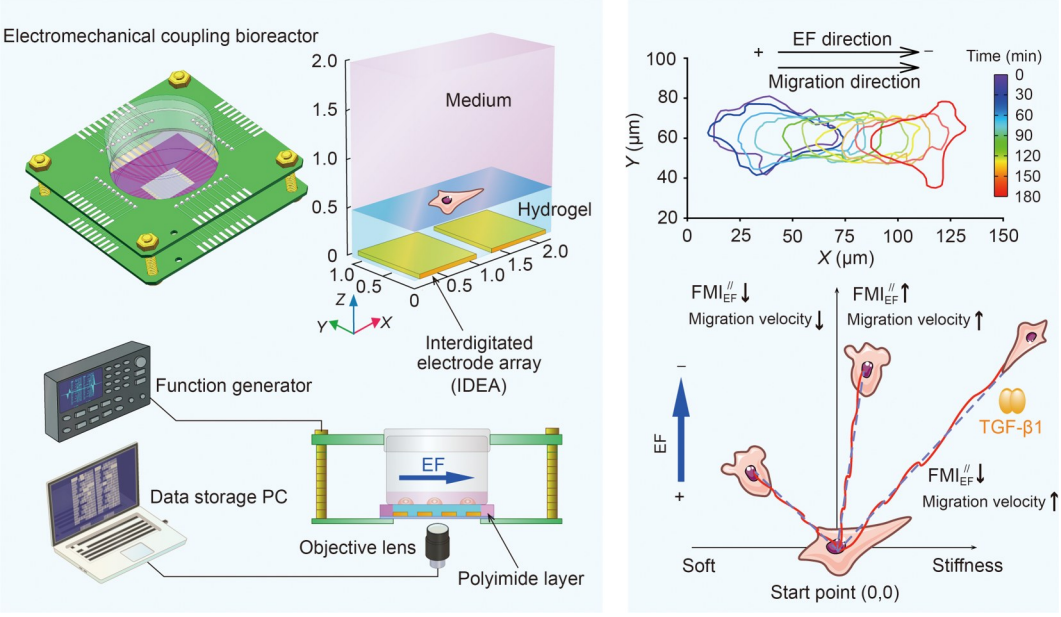

Keywords Electromechanical coupling · Cancer cell directional migration · Stiffness · Cytoskeleton · Transforming growth factor-β1 (TGF-β1)

1 Introduction

Endogenous electric fields (EFs) are nonnegligible biophysical clues in the extracellular space [1–4]. Most organs (especially glands, such as the lung) surrounded by epithelial cells produce potential differences or transepithelial potentials (TEPs). In essence, endogenous EFs are generated from the vectorial transport of ions by cells (especially by TEPs), which forms and maintains asymmetric regional positive and/or negative charge concentration gradients [3, 5]. Due to the different ion-selective transport characteristics of diverse types of epithelial cells that surround various organs (especially glands) in the human body, intertissue EFs are generated [5, 6]. The strength of physiological EFs formed by TEPs can reach several V/cm [7–10]; for example, the value in the rectum and small airways of the lungs can vary in strength from 0.5 to −5.0 V/cm [11–23], sufficient to elicit various cellular responses [7, 10]. Many recent studies have emphasized the critical guiding role of extracellular EFs in embryonic development [24] and tissue regeneration [25], especially in wound healing [26].

Cancers have been considered "wounds that fail to heal" for decades [27]. Extracellular EFs have been detected to exist inside cancer tissues, on the cancer tissue surface, and between cancer tissues and adjacent tissues [28–30]. Mechanistically, compared to normal polarized epithelial cell membranes with distinct apical and basal regions, membranes containing rapidly proliferating cancer cells can be depolarized [3, 31], generating local EFs in cancerous tissue [29, 30]. Cancer progression disrupts the local ionic environment and interferes with the TEP, inducing a difference in the electrical potential between cancer tissues and the adjacent normal tissues [28, 32]. Detection results have shown that the strength of cancer EF can exceed 1 V/cm [33], varying from 1.5 to 23.25 mV across approximately 50 μm [29]. To date, carcinogenesis-triggered EFs correlate strongly with solid tumor size and heterogeneity [29, 31] and can serve as biological markers for cancer diagnosis and prognosis [28–32, 34]. Therefore, EFs may serve as fundamental but poorly understood regulators of cancer progression.

Various EF stimulation devices have been established to mimic endogenous EFs and explore cellular responses to EFs. However, there are still some limitations that must be overcome in these EF stimulation devices. For conventional EF stimulation devices, paired conductive electrodes are introduced through direct immersion into the cell culture medium (e.g., carbon rod, platinum, and stainless-steel electrodes) or are connected to the medium via agar salt bridges (e.g., Ag/AgCl) to excite EFs, resulting in medium evaporation, compromised experimental consistency, and low experimental throughput [7, 35–38]. Recently, a series of

polydimethylsiloxane (PDMS)- and polymethylmethacrylate-based microfluidic devices have been proposed for use in EF stimulation trials in miniaturized devices [7]. These devices can improve conventional EF stimulators in different manners, such as enhancing EF controllability [39], prolonging cell culture time [40], applying electrical/fluid shear stimuli to cells [41], or combining biochemical gradients with electrical stimuli [42]. However, the introduction of microfluidic technology has compromised the convenience of EF stimulation assays and created challenges associated with cell seeding and adhesion [43, 44]. Recently, material-induced EFs have also been applied to electrical stimulus experiments on cells, such as cell-scale confined EFs generated by $K_{0.5}Na_{0.5}NbO_3$ (KNN)-based ceramics via laser-induced phase transition technology [45] and surface Volta potentials generated by bimetals via spark plasma sintering technology [46]. However, these methods are less flexible than conventional electrodes in accurately adjusting EF intensity and distribution, cannot easily generate continuous uniform EFs within the macroscopic plane, and require expensive special equipment and technology. Overall, existing EF stimulation devices cannot balance the convenience and robustness of equipment fabrication while ensuring that EF in a target region is uniform and can be precisely controlled. More importantly, almost all EF-stimulation trials have been conducted by seeding cells on rigid substrates, such as poly(lactic-co-glycolic acid) (PLGA) polymers [47, 48], glass [5, 49], or conventional plastic culture dishes/plates [29, 50, 51]. These materials exhibited Young's moduli in the GPa range, typically 10^3–10^4 times stiffer than those of native ECM [52, 53]. The physiological stiffness information in the ECM was ignored.

Cells sense the mechanical cues present in the ECM and convert them into meaningful biological activities. The mechanical stiffness of the ECM has been recognized to play an essential role in regulating cellular functions, from guiding cell migration to affecting cell differentiation [54, 55]. Changes in ECM stiffness caused by disease or development guide the gene expression and function of cells, which in turn mediate these physiological and pathological processes [56, 57]. Regarding cancer progression, progressive stiffness is among the most recognizable characteristics of cancers and is strongly correlated with the degree of cancer malignancy [58, 59]. Cancer cells can stiffen the ECM by secreting biochemical factors to activate stromal cells, such as cancer-associated fibroblasts, resulting in the excessive deposition of ECM proteins [60]. Besides, cancer progression can lead to the hardening of the ECM by promoting malignant and stromal cell migration, which densifies the ECM by mechanically pulling and recombining ECM fibers [60]. Conversely, a stiffened ECM can activate a series of mechanotransduction pathways (such as the Rho/rock, integrin-related, and phosphatidylinositol 3-kinase (PI3K)/Akt signaling pathways) in cancer cells, which further increases cancer cell malignancy and promotes cancer invasion [1, 36, 61]. However, although mechanical stiffness is a nonnegligible biophysical signal in the cellular microenvironment, further studies are needed to reveal whether and how cells respond to ubiquitous electromechanical coupling signals.

In this study, to bridge the knowledge gap and improve the aforementioned limitations, we developed an electro-stiffness coupling bioreactor that can orthogonally and robustly apply the desired EFs and stiffness stimulations to individual cells across the physiological spectrum. In our electro-stiffness bioreactor, interdigitated microelectrode arrays prepared by lithography were used to apply uniform EFs to cells; fibronectin-modified hydrogels with designed stiffness, which were covalently bonded to the microelectrode array surface, were used to mimic the mechanical environment of the ECM. By delivering orthogonally controlled electro-stiffness coupling signals, our bioreactor revealed that electro-stiffness stimulations shaped cancer cell morphology and cytoskeleton into a distinctive polarization state. Meanwhile, stiffness regulated the sensitivity of cancer cells to EFs. Moreover, cytoskeleton and transforming growth factor-β1 (TGF-β1) mediated the cellular response to the electro-stiffness signals. These findings, along with our bioreactor, helped reveal the underlying biophysical mechanisms of multiple cue-regulated cellular behaviors and established an encouraging foundation for biophysical-based cell control and disease treatment.

2 Results

2.1 Design and fabrication of the electro-stiffness coupling bioreactor

We fabricated an electro-stiffness coupling bioreactor to systematically investigate the cell's response to ubiquitous electromechanical signals in the cellular microenvironment; through this bioreactor, various combinations of EF and stiffness stimuli can be applied to cells across the physiological spectrum (Fig. 1a; Fig. S1 and Sect. S1 in the supplementary information). The core component of our bioreactor is an electro-stiffness-coupled chip that contains an interdigitated electrode array (IDEA), a patterned insulating layer, and a polyacrylamide (PAAm) hydrogel layer whose stiffness can be adjusted within the physiological range. The process used to fabricate the electro-stiffness-coupled chip is shown in Fig. 1b (Sect. S1 in the supplementary information). The IDEA was fabricated from indium tin oxide (ITO) glass by photolithography and wet-etching techniques. A patterned polyimide (PI) layer was modified on the ITO chip using photolithography

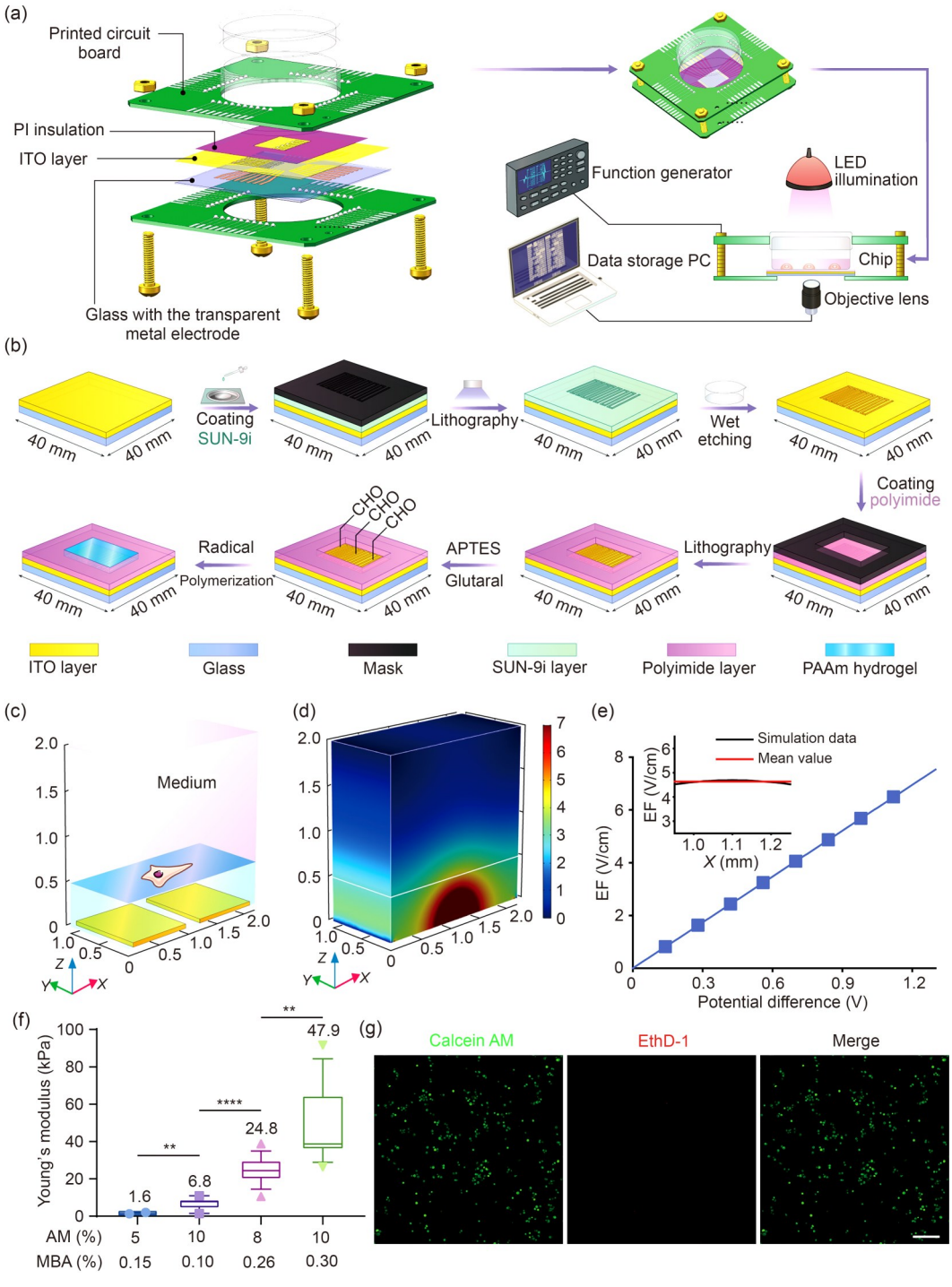

Fig. 1 Fabrication and characterization of the electro-stiffness coupling bioreactor. (a) Schematic diagram showing the structure and experimental setup of the electro-stiffness coupling bioreactor. (b) Schematic illustration depicting the fabrication of the electro-stiffness-coupled chip, which was the core component of our bioreactor. (c) Geometric model of the electro-stiffness coupling bioreactor for applying electromechanical stimulation to cells. The gap between two adjacent ITO electrodes was 100 μm. (d) Spatial distribution of EF generated by the electro-stiffness coupling bioreactor, which was obtained by finite-element simulation. This distribution corresponded to an electric potential difference of 0.8 V applied to two adjacent electrodes. (e) Relationship between EF strength and electric potential differences extracted via finite-element simulation. The partial image shows EF distributions on the upper surface of PAAm hydrogels (black line) and the mean strength (red line) corresponding to EF in (d). (f) Young's moduli of PAAm hydrogels adopted in our electro-stiffness coupling bioreactor with different AM/MBA ratios of 1.6, 6.8, 24.8, and 47.9 kPa. Boxes represent 10th–90th percentiles with median line ($n \geqslant 10$). $^{****}P<0.0001$; $^{**}P<0.01$ (one-way analysis of variance). (g) Live/Dead assay for A549 cells cultured in an electro-stiffness bioreactor. Representative fluorescence images of A549 cells cultured on a 47.9 kPa PAAm hydrogel under an EF of 5.67 V/cm for 3 h are shown. The live and dead cells were stained green and red, respectively. Scale bar: 200 μm. LED: light-emitting diode; PC: personal computer; APTES: 3-aminopropyltrimethoxysilane

technology to form insulation between the electrodes and the culture medium in the nonexperimental area. A quartz ring with a matching lid was firmly adhered to the electro-stiffness-coupled chip by PDMS, forming a cell culture chamber (Fig. 1a; Fig. S1 in the supplementary information). The Young's modulus of the PAAm hydrogel layer can be adjusted by changing the ratio of the monomer to the cross-linker [62], and this layer was introduced to the IDEA surface to provide a physiologically stiff environment for cells (Sect. S2 and Table S1 in the supplementary information). To prevent the PAAm hydrogel from drifting during EF stimulation, the surface of ITO chips was functionalized with the aldehyde group, which can react with the amino group of the PAAm molecule and covalently immobilize the PAAm hydrogel on the IDEA surface, as shown in Fig. 1b (Sect. S1 in the supplementary information). The PAAm hydrogel surface was modified with fibronectin (Sect. S1 in the supplementary information), providing cells with an adhesion environment mimicking the native ECM. Finally, by connecting the electro-stiffness coupling chip to the function generator through a printed circuit board (PCB), a complete electro-stiffness bioreactor was established (Fig. 1a). Before use, the bioreactor was sterilized by ultraviolet (UV) irradiation. In the experiments, cells were seeded on the surface of functionalized PAAm hydrogel layers, and the electrobioreactor connected to the functional generator was placed into a live-cell workstation to record the spatiotemporal dynamics of cells in real time (Fig. 1a).

In our experiments, specific EFs applied to cells via the electro-stiffness bioreactor were characterized based on electrochemical workstation measurements combined with finite-element simulations, and the stiffness of PAAm layers was characterized using a nanoindenter (Piuma, The Netherlands). As shown in Figs. 1c and 1d, a finite-element model was established according to the actual size and position relationship between the ITO electrodes and PAAm hydrogel combined with the electrical parameters of the electro-stiffness bioreactor measured by the electrochemical workstation (Figs. S2–S5, Sect. S3, and Table S2 in the supplementary information). Results showed that the IDEA can generate a uniform EF in the cell spreading area on the PAAm hydrogel surface. Specifically, a series of uniform EFs with intensities of 0.81, 1.62, 2.43, 3.24, 4.05, 4.86, and 5.67 V/cm can be applied to cells via the electromechanical bioreactor by applying corresponding potential differences of 0.14, 0.28, 0.42, 0.56, 0.70, 0.84, and 0.98 V on ITO microelectrodes, respectively (Figs. 1d and 1e; Fig. S6 and Table S3 in the supplementary information). The typical distribution of EF in the bioreactor is shown in Fig. 1d when the electric potential difference applied to the two adjacent electrodes was 0.84 V. The representative distribution of EF (electric potential difference: 0.84 V) on the upper surface of the PAAm hydrogel layer was extracted and illustrated in the partial view of Fig. 1e. In this figure, our bioreactor can form a uniform EF to stimulate cells adhering to the PAAm hydrogel layer. The Young's modulus of PAAm hydrogels adopted in our electro-stiffness bioreactor was controlled by adjusting the ratio of the monomer (acrylamide monomer (AM)) to the cross-linker (N,N′-methylenebis-acrylamide (MBA)). As shown in Fig. 1f, PAAm hydrogels with stiffnesses of 1.6, 6.8, 24.8, and 47.9 kPa were prepared by adjusting the AM/MBA proportions to 5%/0.15%, 10%/0.10%, 8%/0.26%, and 10%/0.30%, respectively. Specifically, for lung cancer cells used in this study, 1.6 kPa was selected to represent the stiffness of normal human lung tissue [63, 64], whereas 6.8, 24.8, and 47.9 kPa were chosen to represent the stiffness of gradually hardening lung cancer tissues [65, 66]. A live/dead assay for A549 cells cultured in our electro-stiffness bioreactor demonstrated that at the stiffness of PAAm hydrogels of 1.6, 6.8, 24.8, and 47.9 kPa, the constructed bioreactor could maintain high cell viability (Fig. 1g; Fig. S7 in the supplementary information). Overall, our bioreactor can apply freely integrated and precisely controlled electro-stiffness coupling signals to cells, which explores the relationship between electromechanical cues and cellular behavior via real-time visualization and quantitative analyses at the single-cell level.

2.2 Electro-stiffness coupling signals are guidance cues to direct cancer cell orientation and migration

Although stiffness plays a significant role in cellular function and behavior, almost all electrical stimulation tests have been conducted on rigid substrates, such as glass [5, 49] and plastic Petri dishes and plates [2, 29, 50, 51, 67], whose Young's moduli (several GPa) were generally at least several orders of magnitude stiffer than those of native ECM [52, 53]. In this study, based on the above electro-stiffness coupling bioreactor we designed, we first investigated the effects of EFs on cancer cells on PAAm hydrogels with Young's modulus of 24.8 kPa, the typical stiffness of human lung cancer tissues [65, 66]. Because the TEP observed in lung tissues was characterized as a direct current (DC) EF with intensities from 0.3 to 5.0 V/cm, DC electrical stimuli at intensities of 0.81, 1.62, 2.43, 3.24, 4.05, 4.86, and 5.67 V/cm were employed for A549 cell treatment.

The electro-stiffness coupling environment can shape the cytoskeleton into a unique anteroposterior polarization state. Figure 2a and Fig. S8 (supplementary information) show that under cancer-specific stiffness conditions (24.8 kPa), EF stimulation significantly reduced A549 cell spreading and induced obvious anteroposterior polarity of the A549 cytoskeleton. The pseudopodium formation and polarization of the F-actin cytoskeleton are crucial for cell

migration [68]. As shown in Fig. 2a, after A549 cells were seeded on 24.8 kPa substrates with EF stimulation of 5.67 V/cm for 3 h, cells specifically protruded broad sheet-like lamellipodia at the front edge of migrating cells in the direction of movement. In contrast, the corresponding rear edge exhibited a smooth arc-like shape without any lamellipodia and showed a highly EF-polarized cytoskeleton, significantly different from the cytoskeleton of unstimulated cells that contained randomly distributed pseudopods (including lamellipodia and filopodia) (the control group in Fig. 2a and Fig. S8 in the supplementary information). Consistently, Fig. 2b shows the real-time contour changes of A549 cells stimulated by EF at 24.8 kPa PAAm for 180 min, revealing that the dynamic change in cell morphology varied from a polygon to a typically polarized contour. Statistically, as shown in Fig. S8 (supplementary information), the spread area and aspect ratio (AR) of A549 cells decreased significantly with the time of EF induction, and the circularity of A549 cells increased significantly with the time of EF induction, further demonstrating that electro-stiffness coupling signals induced cell polarization and significantly changed the cellular morphology. In summary, the abovementioned assays demonstrated that cancer cells sense and respond to physiological electro-stiffness signals by exhibiting a particular EF-polarized cytoskeleton and morphology.

We established a Cartesian coordinate system to describe cell migration in our bioreactor. In this system, the origin was defined as the initial position of the cell, and the *Y*-axis direction was defined as the direction of EF, which was termed the EF-induced direction (EFID) (Fig. 2c). A549 cells cultured on the surface-modified PAAm hydrogel did not penetrate the internal structure of hydrogels, so only the movement trajectory of A549 cells in the *XY* plane was analyzed. Based on the Cartesian coordinate system, the migration trajectories of ⩾50 cells are shown in Fig. 2d. Figure 2d clearly shows that on the physiological stiffness matrix (24.8 kPa), EF-stimulated A549 cells exhibited directional migration along the EFID, whereas A549 cells not stimulated by EF showed random migration without any orientation preference. To further quantify cell locomotion, several migration indices (i.e., forward migration index (FMI), migration velocity, mean square displacement (MSD), and β index) were calculated based on the Cartesian coordinate system established above. FMI, which was calculated

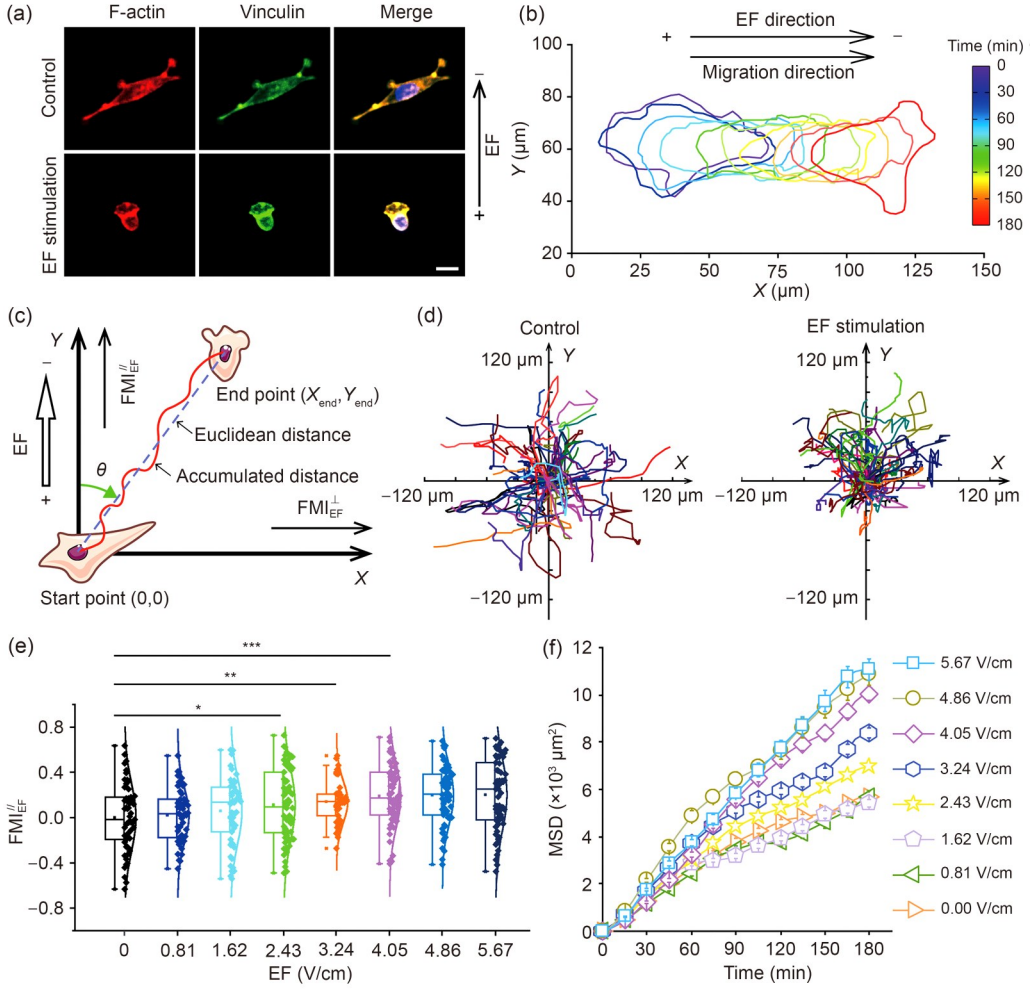

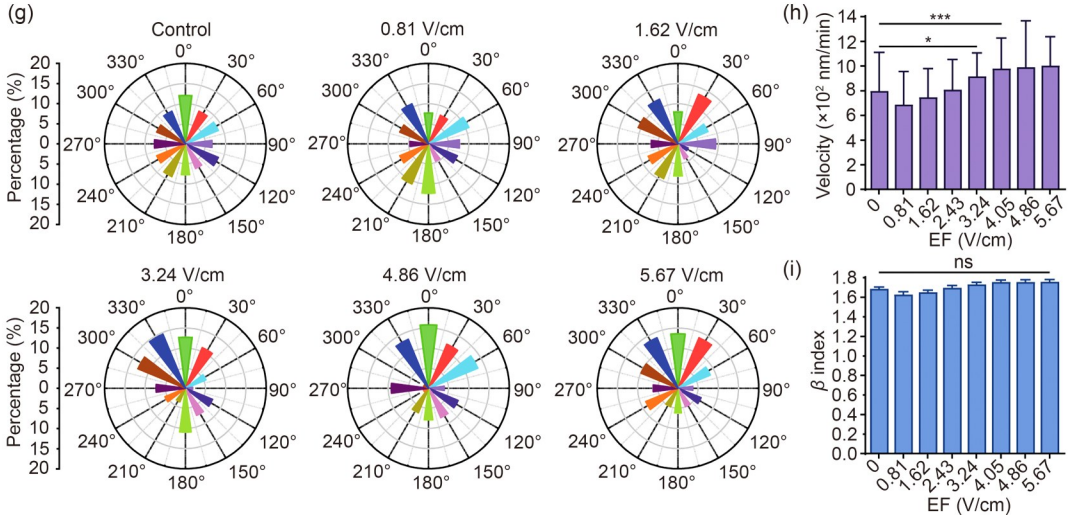

Fig. 2 EF-induced cancer cell polarization and directional migration under stiffness conditions specific to cancer. (a) Representative fluorescence images of A549 cells stimulated with EF (5.67 V/cm) on the PAAm hydrogel at 24.8 kPa for 3 h. The control group included cells cultured on the PAAm hydrogel at 24.8 kPa without EF stimulation. The arrow on the right side is the EF direction. Red, F-actin; green, vinculin; blue, nuclei. Scale bar: 20 μm. (b) Contour changes of A549 cells under stimulation with EF (5.67 V/cm) for 3 h. The colors and coordinate positions of the cell contours represent the induction time and migration trajectories, respectively. (c) Definition of the Cartesian coordinate system and reference directions used to describe cell migration. The dotted dashed line is the Euclidean distance between the starting and end points of a cell, and the solid line is the accumulated distance of the cell migration path. The positive direction of the *Y*-axis is defined as the EF direction. The reference directions of $FMI_{EF}^{\perp}$ and $FMI_{EF}^{/\!/}$ are perpendicular and parallel to the direction of EF, respectively. θ is defined as the angle between the start–end line of migrating cells and the positive direction of the *Y*-axis. The θ index gradually increases in the clockwise direction. (d) Statistics of cell migration trajectories under free migration (control) and EF induction (5.67 V/cm) conditions, $n \geqslant 50$. (e) Box-scatter plot showing the $FMI_{EF}^{/\!/}$ of A549 cells at EFs of 0, 0.81, 1.62, 2.43, 3.24, 4.05, 4.86, and 5.67 V/cm, $n \geqslant 33$. $^{***}P<0.001$; $^{**}P<0.01$; $^{*}P<0.1$ (*t*-test). (f) Line plot showing the change in mean square displacement (MSD) over time at EFs of 0, 0.81, 1.62, 2.43, 3.24, 4.05, 4.86, and 5.67 V/cm, $n \geqslant 33$. (g) The wind rose plots display the angular distributions of θ under EF stimulation for 3 h at densities of 0, 0.81, 1.62, 3.24, 4.86, and 5.67 V/cm, $n \geqslant 30$. Bar plots representing the quantitative data of velocity (h) and β index (i) of A549 cells on the PAAm hydrogel at 24.8 kPa at EFs of 0, 0.81, 1.62, 2.43, 3.24, 4.05, 4.86, and 5.67 V/cm, $n \geqslant 33$. $^{***}P<0.001$; $^{*}P<0.1$; ns: not significant (*t*-test). Data in (e) express the maximum, minimum, median, and upper and lower quartiles of a set of data. Data in (f) are expressed as mean±standard error of the mean. Data in (h, i) are expressed as mean±standard deviation

based on Eq. (1) in Sect. 4, is the ability of cells to directionally migrate under the elicitation of exogenously induced signals, the reference direction of which can be set parallel ($FMI_{EF}^{/\!/}$) or perpendicular ($FMI_{EF}^{\perp}$) to EF direction. As shown in Fig. 2e, for PAAm hydrogels with stiffness that mimicked that of real lung cancer tissues, the $FMI_{EF}^{/\!/}$ index of A549 cells nonlinearly increased with increasing EF intensity, reaching a plateau with a peak value of 0.191±0.272 at EF=4.05 V/cm. In contrast, the $FMI_{EF}^{\perp}$ of A549 cells under the same experimental conditions remained near zero. Thus, cells always showed nonoriented locomotion in the direction perpendicular to EFID (Fig. S9 in the supplementary information). Combining the statistical data of $FMI_{EF}^{/\!/}$ and $FMI_{EF}^{\perp}$, it can be concluded that A549 cells exhibited directional migration along the EFID, and this direct migration can be promoted by increasing EF intensity. Moreover, as shown in Figs. 2h, 2f, and 2i, we calculated the migration velocity (*V*), MSD, and β index of A549 cells based on Eqs. (2)–(4) in Sect. 4. As shown in Fig. 2h, the migration velocity (*V*) of A549 cells increased significantly with the elevation of EF strength. Compared to the speed and directionality, the persistence of A549 migration was relatively less affected by EFs. The change rate of MSD over time (i.e., slope of the MSD–time curve) can be used to characterize the persistence of cell migration. As shown in Fig. 2f, during electrical stimulation, the slope of the MSD–time curve of A549 cells showed an increasing trend with the increase of EF intensity, especially after 1-h electrical stimulation. However, despite the β index (another migration persistence indicator) of A549 cells showing a slight upward trend as the EF strength increased from 0.81 to 5.67 V/cm, their values showed no statistical difference compared to the control group. Overall, under cancer-specific stiffness conditions, EFs exhibited a significant strength-dependent directional induction effect on A549 migration while promoting migration speed but not persistence.

To further verify the directional induction effect of EFs on A549 cell migration, we analyzed the change in the position of A549 cells relative to EFID after EF stimulation, which is described as the angle (θ) between the origin–end vector of the cell and EFID. The θ index gradually increased

in the clockwise direction (Fig. 2c). Consistently, the statistics showed that the end points of cells were almost evenly distributed in all directions without EF stimulation, whereas the end points of cells were gradually distributed along the EFID with increasing EF intensity (Fig. 2g). In summary, the above results demonstrated that electro-stiffness coupling signals can shape cancer cells into a unique anteroposterior polarized state, and the directional migration of cancer cells can be induced and promoted by EFs under typical cancer stiffness conditions.

2.3 Stiffness regulates cancer cell susceptibility to electrical stimulation in a synergistic manner

Cells perceive the stiffness signals of the ECM and translate them into meaningful biological activities through mechanotransduction pathways. Progressive stiffness is among the most recognizable characteristics of cancers and has recently been recognized to play an important role in cancer progression and metastasis. Therefore, it is necessary to investigate the effect of stiffness on EF-induced cancer cell behavior. To this end, A549 cells, which are typical lung cancer cells, were cultured in bioreactors with PAAm hydrogels to mimic Young's modulus of normal lung tissues (1.6 kPa) and gradually harden lung cancer tissues (6.8, 24.8, and 47.9 kPa) [64–66].

Our experiments showed that stiffness regulates the EF-induced polarization of A549 cells. Figure 3a shows representative immunofluorescence images of A549 cells cultured on PAAm hydrogels with different stiffnesses in the free-spreading state (control group) and EF-induced state, which further confirms the following conclusion: under physiological stiffness, EF stimulations can significantly reduce cellular spread and induce a unique anteroposterior polarization morphology in cells. More importantly, as shown in Fig. 3a, the number and area of broad sheet-like lamellipodia protruding from cancer cells at the front of cells increased with increasing substrate stiffness, whereas the corresponding rear edge mainly maintained a smooth arc-like shape without any lamellipodia, showing that EF-induced cell polarization was promoted by increasing stiffness. Consistently, as shown in Fig. S10 (supplementary information), the circularity of A549 cells decreased by 38.71% when the substrate stiffness increased from 1.6 to 24.8 kPa under an EF stimulation of 5.67 V/cm, and the aspect ratio of A549 cells improved by 21.43% when the substrate stiffness increased from 1.6 to 24.8 kPa under an EF stimulation of 5.67 V/cm. Overall, the above results indicated that stiffness exerted a regulatory effect on EF-induced cell polarization.

To explore the regulatory effect of stiffness on the oriented locomotion of cancer cells induced by the EF, we obtained statistics on the end point distribution of A549 cells relative to EFID under different stiffness conditions. As shown in Fig. 3b, a growing number of cells gathered in EFID with increasing substrate stiffness. Specifically, after EF stimulation at 5.67 V/cm for 3 h, the proportion of A549 cells distributed in the spatial region of $(-45°, +45°)$ was approximately 43% on 47.9 kPa gels, whereas the corresponding value decreased to about 24% on 1.6 kPa gels. Overall, Fig. 3b shows that with increasing substrate stiffness, cancer cells moved more toward EF. Consistently, as shown in Fig. 3c, the $FMI^{//}_{EF}$ of A549 cells varied from 0.094 ± 0.306 to 0.216 ± 0.213 when the substrate stiffness increased from 1.6 to 47.9 kPa, further demonstrating that substrate stiffness regulates the ability of EFs to promote the direction that cancer cells migrate. There was no significant difference in $FMI^{//}_{EF}$ between the control and 1.6 kPa EF stimulation groups (Fig. 3c), indicating that a certain stiffness threshold was necessary for directional cell migration induced by EFs. Moreover, as shown in Figs. 3d–3f, indices of cell migration speed (i.e., velocity) and persistence (i.e., change rate of MSD over time and β index) exhibited an increasing trend with increasing matrix stiffness, demonstrating that increasing stiffness promotes the EF-induced ability of cancer cells to directly migrate. To further describe the correlations between the stiffness and EFID migration of cancer cells, phase diagrams of migration indices (i.e., $FMI^{//}_{EF}$, velocity, and β index) under different electro-stiffness coupling signals were drawn (Figs. 3g–3i). As shown in Fig. 3g and Fig. S11 (supplementary information), when the substrate stiffness exceeded about 24.8 kPa, the $FMI^{//}_{EF}$ increased significantly with increasing EF intensity, whereas $FMI^{//}_{EF}$ did not significantly change with increasing EF intensity when the stiffness was <6.8 kPa. Similarly, as shown in Figs. 3h and 3i and Fig. S11 (supplementary information), on hydrogels with relatively high moduli, EF exhibited a significant promoting effect on the migration ability of cancer cells, including the migration velocity (V) and migration persistence (β index); however, on soft hydrogels, the migration velocity (V) and migration persistence (β index) showed weak sensitivity to EF intensity. In summary, increasing stiffness amplified the induction effect of EFs on cancer cells, including stimulating cell polarization and directional migration, which explained how stiffness promoted cancer cell migration and metastasis from an electromechanical perspective.

2.4 The cytoskeleton modulates the directional migration of cancer cells induced by electro-stiffness coupling signals

The cytoskeleton is indispensable for cell motility and the maintenance of cell morphology. Based on our bioreactor, electro-stiffness coupling signals induced cell polarization and directional migration, which involved lamellipodia

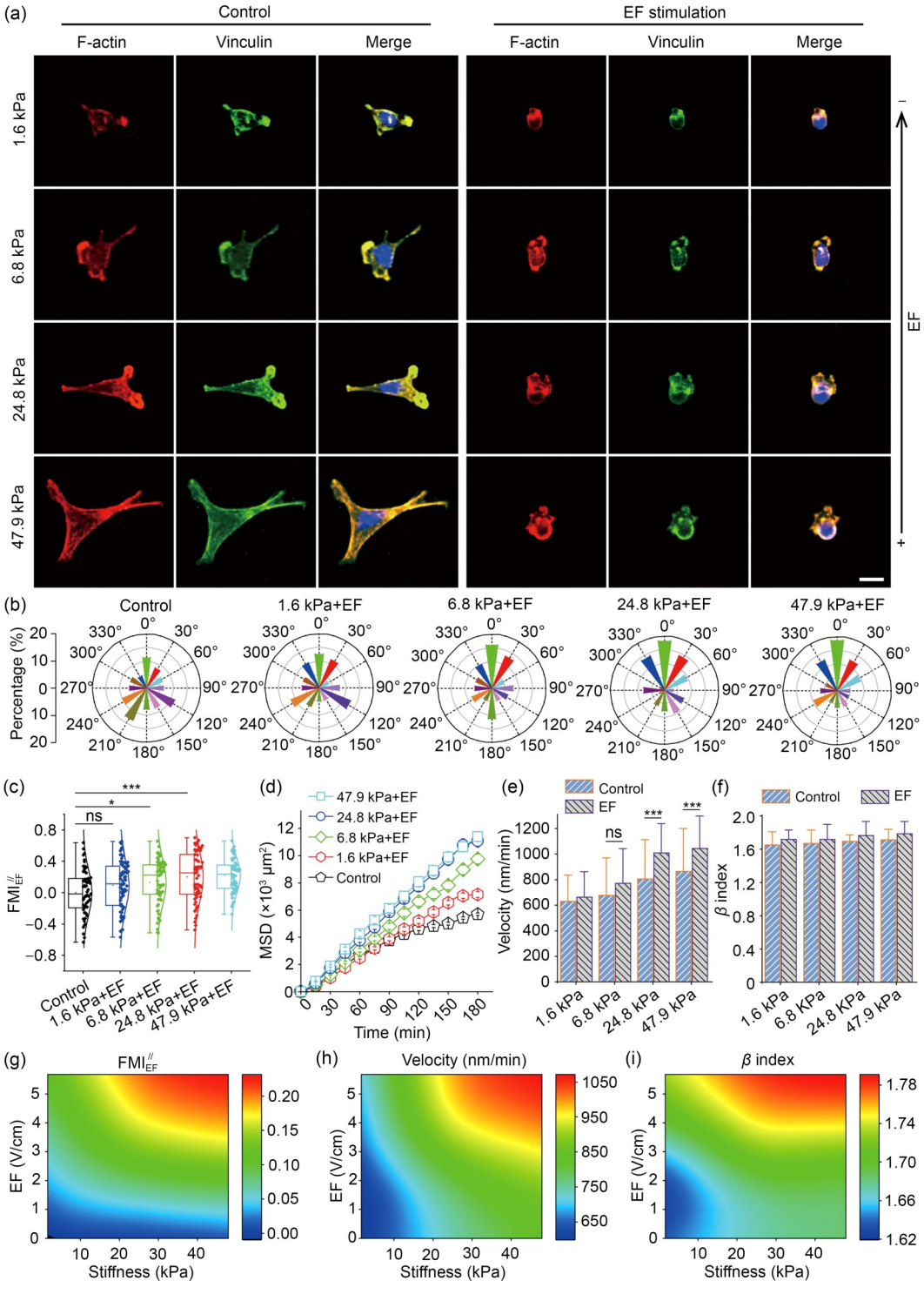

Fig. 3 Stiffness regulates the sensitivity of EF-induced polarization and directional migration of cancer cells. (a) Representative fluorescence images of A549 cells cultured on PAAm hydrogels (1.6, 6.8, 24.8, and 47.9 kPa) under the elicitation of an EF (5.67 V/cm). The control group included cells on PAAm hydrogels (1.6, 6.8, 24.8, and 47.9 kPa) without EF stimulation. The arrow on the right side is the EF direction. Red, F-actin; green, vinculin; blue, nuclei. Scale bar: 20 μm. (b) The wind rose plots display the angular distributions of θ under EF stimulation for 3 h on PAAm hydrogels with stiffnesses of 1.6, 6.8, 24.8, and 47.9 kPa. The randomly moving cells in the control group were seeded on the PAAm hydrogel at 24.8 kPa without EF induction, $n \geq 30$. Statistical results of $FMI^{//}_{EF}$ (c), MSD (d), velocity (e), and β index (f) of A549 cells under 5.67 V/cm EF induction on PAAm hydrogels with stiffnesses of 1.6, 6.8, 24.8, and 47.9 kPa, $n \geq 30$. $^{***}P<0.001$; $^{*}P<0.1$; ns: not significant (t-test). Phase diagrams of $FMI^{//}_{EF}$ (g), velocity (h), and β index (i) of A549 cells under stimulation with various combinations of EFs and stiffness, $n \geq 30$. Data in (c) express the maximum, minimum, median, and upper and lower quartiles of a set of data. Data in (d) are expressed as mean±standard error of the mean. Data in (e, f) are expressed as mean±standard deviation

protrusions mainly concentrated in EFID (Fig. 3a). Therefore, it is reasonable to hypothesize that the cytoskeleton helps regulate EFID migration under physiological stiffness conditions.

To verify this hypothesis, we used cytoskeleton-regulating drugs to investigate the electro-stiffness-mediated directionality migration of A549 cells (Fig. 4). We first investigated the effect of cytoskeletal inhibitors. Cytochalasin D (CytoD) is a widely used microfilament inhibitor. CytoD of 0.01 μmol/L began to inhibit actin polymerization, and CytoD above 1.0 μmol/L began to affect A549 cell viability [69–74]. To investigate the role of the actin filament in the EFID migration of A549 cells, CytoD with concentration gradients of 0.01, 0.1, 0.5, and 1.0 μmol/L was

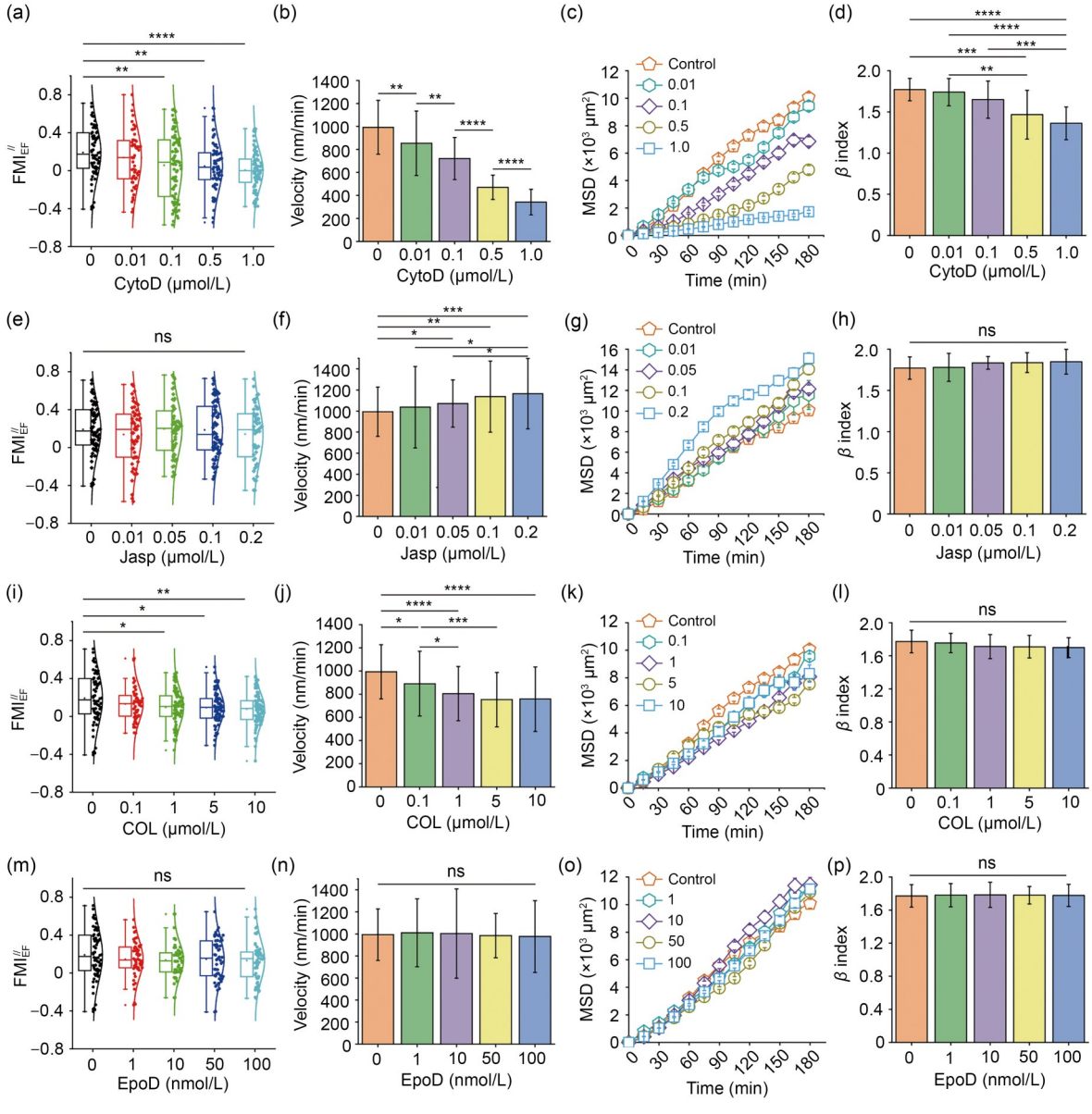

Fig. 4 Modulatory effect of the cytoskeleton on the directional migration of cancer cells under electro-stiffness coupling stimulation. (a–d) Statistical analysis of directional migration indices ($FMI^{//}_{EF}$, velocity, MSD, and β index) of A549 cells treated with CytoD (microfilament inhibitor) at 0, 0.01, 0.1, 0.5, and 1.0 μmol/L, $n \geq 48$. $^{****}P<0.0001$; $^{***}P<0.001$; $^{**}P<0.01$ (*t*-test). (e–h) Statistical analysis of the directional migration indices ($FMI^{//}_{EF}$, velocity, MSD, and β index) of A549 cells treated with Jasp (microfilament stabilizer) at 0, 0.01, 0.05, 0.1, and 0.2 μmol/L, $n \geq 33$. $^{***}P<0.001$; $^{**}P<0.01$; $^{*}P<0.1$; ns, nonsignificant (*t*-test). (i–l) Statistical analysis of the directional migration indices ($FMI^{//}_{EF}$, velocity, MSD, and β index) of A549 cells treated with COL (microtubule inhibitor) at 0, 0.1, 1, 5, and 10 μmol/L, $n \geq 51$. $^{****}P<0.0001$; $^{***}P<0.001$; $^{**}P<0.01$; $^{*}P<0.1$; ns, nonsignificant (*t*-test). (m–p) Statistical analysis of directional migration indices ($FMI^{//}_{EF}$, velocity, MSD, and β index) of A549 cells treated with EpoD (microtubule stabilizer) at 0, 1, 10, 50, and 100 nmol/L, $n \geq 45$. ns: not significant (*t*-test). Data in (a, e, i, m) express the maximum, minimum, median, and upper and lower quartiles of a set of data. Data in (b, d, f, h, j, l, n, p) are expressed as mean±standard deviation. Data in (c, g, k, o) are expressed as mean±standard error of the mean

used. As shown in Fig. 4a, the $FMI^{//}_{EF}$ of A549 cells decreased sharply with increasing CytoD concentration, indicating that the inhibition of actin microfilaments significantly weakened the EF-induced orientation of cancer cell movement. The migration velocity (V) and persistence (i.e., change rate of MSD over time and β index) also decreased significantly with the increase of the actin microfilament inhibition (Figs. 4b–4d). Similarly, we quantified the influence of colchicine (COL), a widely used microtubule inhibitor and disruptor [75, 76]. The dose response of A549 to COL has been previously determined, and 5 μmol/L was considered the optimal COL concentration [77]. COL at 1–6.26 μmol/L has been used to regulate various microtubule-mediated physiological activities of A549 cells [71, 78, 79], which began to affect the microtubule-mediated mechanical properties of cancer cells at 0.1 μmol/L and reached a plateau at 10 μmol/L [80]. In this study, COL with concentration gradients of 0.1, 1, 5, and 10 μmol/L was used to investigate the role of microtubules in the EFID migration of A549 cells. As shown in Figs. 4i–4l, although the persistence of cell migration was not affected, microtubule inhibition simultaneously weakened the directionality and speed of cancer cell migration. Overall, cytoskeleton inhibition significantly suppressed the electro-stiffness-mediated directionality of A549 migration.

Contrary to CytoD, jasplakinolide (Jasp) is an effective stabilizer for actin filaments. Jasp (0.05–0.125 μmol/L) has been used to effectively induce actin polymerization in A549 cells [74, 81]. In this study, 0.01, 0.05, 0.1, and 0.2 μmol/L Jasp were used to explore the EFID migration of A549 cells. As shown in Figs. 4e–4h, although Jasp significantly promoted the migration ability of A549 cells, it did not affect the directionality of electromechanical-mediated A549 cell migration. This seemingly contradictory phenomenon might be due to the two separable effects of Jasp on filamentous actin. Specifically, Jasp could rapidly block the lamellipodia protrusion of migrating cells within minutes, whereas the significant actin assembly induced by Jasp was delayed until 1 h later [82]. Considering our observation that electro-stiffness signals induce cell polarization by promoting lamellipodia protrusion at the cell front (Sect. 2.2), we speculated that the reason why Jasp cannot further promote the electro-stiffness-mediated directionality of A549 migration is its inhibition of lamellipodia protrusion. Therefore, we stained the cytoskeleton of A549 cells treated with 0.2 μmol/L Jasp. As shown in Fig. S12 (supplementary information), Jasp obviously reduced the area of the electro-stiffness-induced lamellipodia in the anterior part of A549. In essence, this phenomenon was due to the inhibition of cytoskeletal dynamics by stable microfilaments, which further validated our conclusion in Sect. 2.2 that lamellipodia are a key effector for electromechanical-mediated cancer cell polarization. To further validate this conclusion, we identified another cytoskeletal stabilizer that can also inhibit lamellipodia protrusion, namely epothilone D (EpoD). EpoD is a potent microtubule stabilizer demonstrated to improve microtubule density [83]. EpoD (1–100 nmol/L) has been selected to investigate the mediating effect of microtubules on malignant cells, suggesting that EpoD acts on various carcinoma cells in similar concentrations [84–86]. In our experiments, EpoD at 1, 10, 50, or 100 nmol/L was used. As shown in Figs. 4m–4p, the microtubule stabilizer EpoD did not affect A549 cell migration, including the migration ability and directionality. As shown in Fig. S12 (supplementary information), EpoD also inhibited the lamellipodia protrusion of A549 cells under this electro-stiffness condition, consistent with the effect of Jasp. Overall, these data based on cytoskeletal stabilizers emphasized the importance of lamellipodia protrusion in the EFID migration of cancer cells.

In summary, inhibiting the cytoskeleton (including actin microfilament and microtubules) can significantly suppress the directionality of cancer cell migration under electro-stiffness conditions, whereas stabilizing the cytoskeleton barely produces any effect. These results confirmed the involvement of the cytoskeleton in the EFID migration of cancer cells and emphasized that lamellipodium was a key effector in this process.

2.5 TGF-β1 disentangles the directionality and velocity of the electro-stiffness-induced migration of cancer cells

TGF-β1 is a key biochemical component in the tumor microenvironment (TME), which regulates a series of cancer and stromal cell activities during malignant progression, including invasion, metastasis, and immune escape [87, 88]. Although the essential role of biochemical signals in cancer progression has been extensively explored, the combined effect of biophysical and biochemical signals remains mysterious. In this study, we explored the effects of biochemical–electromechanical coupling signals on cancer cells by treating cells with TGF-β1 in our electromechanical bioreactor.

TGF-β1 suppressed the cancer cell orientation induced by the electro-stiffness coupling signals, including cellular polarized morphology and directional migration. As shown in Fig. 5a, a polarization morphology (i.e., large areas of sheet-like lamellipodia converged at the leading edge of the migration direction, whereas the trailing edge of the cell showed nearly no pseudopodia) was electromechanically induced in A549 cells without TGF-β1 treatment, whereas TGF-β1 treatment led to the gradual extension of spiky pseudopodia posterior to cells. Specifically, with increasing TGF-β1 concentration, the number of sheet-like lamellipodia that stretched from the front of cancer cells gradually

decreased, whereas the smooth curved shape of the other parts of cancer cells was gradually replaced by filamentous pseudopodia (Fig. 5a). In addition to altering the polarization state of cancer cells, TGF-β1 inhibited the directivity of the electromechanically stimulated cancer cell migration. As shown in Fig. 5b, the $FMI^{//}_{EF}$ of A549 cells decreased significantly with increasing TGF-β1 concentration. This conclusion was further confirmed by Fig. 5g, which showed that TGF-β1 suppressed the EF-induced migration directionality of A549 cells across the physiological stiffness range. Consistently, after electro-stiffness signals (24.8 kPa, 5.67 V/cm) were induced for 3 h, the end points of A549 cells were gradually distributed in all directions with increasing TGF-β1 concentration, whereas the end points of A549 cells without TGF-β1 treatment were distributed mainly in EF direction (Fig. 5f). In general, TGF-β1 suppressed the

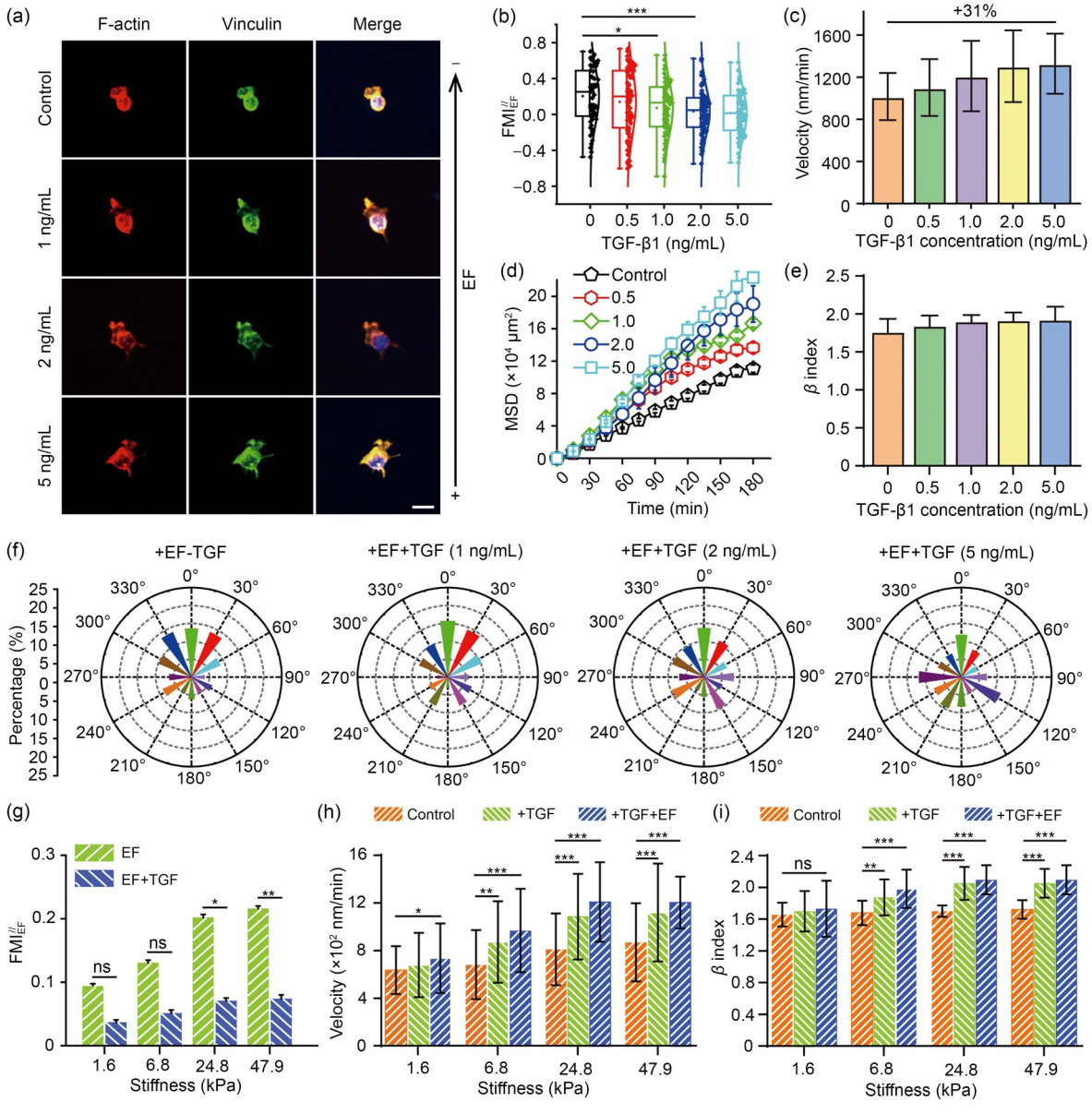

Fig. 5 TGF-β1 suppresses the orientation of cancer cells induced by electro-stiffness coupling signals while simultaneously promoting cancer cell migration. (a) Representative fluorescence images of A549 cells cultured on 24.8 kPa PAAm hydrogels under 5.67 V/cm EF and treated with 0, 1, 2, or 5 ng/mL TGF-β1. The arrow on the right side is the EF direction. Red, F-actin; green, vinculin; blue, nuclei. Scale bar: 20 μm. Statistical analysis of $FMI^{//}_{EF}$ (b), velocity (c), MSD (d), and β index (e) of A549 cells under 5.67 V/cm EF induction on 24.8 kPa PAAm hydrogels treated with TGF-β1 at 0, 1, 2, and 5 ng/mL. (f) Wind rose plots displaying the θ distributions of A549 cells treated with TGF-β1 at 0, 1, 2, and 5 ng/mL under 5.67 V/cm EF stimulation on 24.8 kPa PAAm hydrogels, $n \geq 30$. Statistical results of $FMI^{//}_{EF}$ (g), velocity (h), and β index (i) of A549 cells treated with 1 ng/mL TGF-β1 under 5.67 V/cm EF stimulation on PAAm hydrogels with stiffnesses of 1.6, 6.8, 24.8, and 47.9 kPa, $n \geq 30$. $^{***}P<0.001$; $^{**}P<0.01$; $^{*}P<0.1$; ns: not significant (*t*-test). Data in (b) express the maximum, minimum, median, and upper and lower quartiles of a set of data. Data in (d) are expressed as mean±standard error of the mean. Data in (c, e, g, h, i) are expressed as mean±standard deviation

orientation induction effect of the electro-stiffness coupling stimulation on cancer cells.

Although TGF-β1 inhibited the directionality of cancer cell movement induced by electro-stiffness coupling stimulation, it simultaneously enhanced the migration ability (i.e., velocity and persistence) of cancer cells, demonstrating that the migration ability and directionality of cancer cells can be independently regulated. As shown in Fig. 5c, the migration velocity of A549 cells increased significantly with increasing TGF-β1 concentration. Specifically, the migration velocity of A549 cells increased by 31% when the TGF-β1 concentration increased from 0 to 5 ng/mL (Fig. 5c). As shown in Fig. 5d, the change rate in MSD over time was positively correlated with TGF-β1 concentration under electro-stiffness coupling stimulation, indicating that TGF-β1 promoted the persistence of cancer cell migration in response to electro-stiffness signals. This conclusion is also indirectly supported by Fig. 5e, which showed that the β index of A549 cells under electro-stiffness stimulation increased with increasing TGF-β1 concentration.

Stiffness regulated the suppression effect of TFG-β1 on the EF-induced orientation of A549 cells. Compared to the stiffness of healthy tissues, TGF-β1 did require higher stiffness to effectively suppress the orientation effect of EF on A549 cells. In this study, the orientation effect of EF on A549 cells was manifested in two aspects: one was the anteroposterior polarization of the cytoskeleton, and the other was the directionality of cell migration. As shown in Fig. S13 (supplementary information), under the condition of healthy tissue stiffness (1.6 kPa), TGF-β1 could hardly change A549 cell morphology and the anteroposterior polarity of the cytoskeleton. Only when the TGF-β1 concentration was higher than 5 ng/mL, A549 cells were likely to exhibit extremely tiny filamentous pseudopodia. In contrast, as shown in Fig. 5a, under cancer-specific stiffness conditions (24.8 kPa), 1 ng/mL TGF-β1 was sufficient to alter the cell morphology and polarity and induce the formation of obvious filamentous pseudopodia. Consistently, as shown in Fig. 5g, at the stiffness of healthy tissue (1.6 kPa) and early cancer (6.8 kPa), TGF-β1 addition did not have a statistically significant effect on the $FMI^{/\!/}_{EF}$ of A549 cells; however, at higher stiffness conditions (24.8 and 47.9 kPa), TGF-β1 addition significantly inhibited the $FMI^{/\!/}_{EF}$ of A549 cells. Overall, compared to the stiffness of healthy tissues, increasing stiffness was beneficial for promoting the orientation–inhibition effect of TGF-β1.

In summary, increased stiffness promoted the inhibitory effect of TGF-β1 on EF-induced cell orientation (Fig. 5g) and amplified the acceleration effects of TGF-β1 on EF-facilitated cell migration ability (Figs. 5h and 5i). That is to say, the above data demonstrated that the directionality and ability of cancer cell migration were two independent parameters, and TGF-β1 can exert opposite effects on the directionality and velocity of cancer cell migration, indicating a promising application of our electro-stiffness bioreactor for cell manipulation.

3 Discussion and conclusions

Cells live in a multiphysics-coupled microenvironment containing EFs and mechanical cues. The endogenous electrical potential difference, which exists inside cancer tissues, on the cancer tissue surface, and between cancer tissues and adjacent tissues, has been reported to be a marker for the clinical diagnosis of cancers [28, 29, 32]. Meanwhile, external artificial EFs have shown excellent therapeutic effects in cancer treatment [89, 90]. To date, although numerous studies have investigated EF-guided cell behaviors [2, 67], the mechanical stiffness of the extracellular microenvironment has not been addressed. To dissect the cellular response to these coupling cues, we developed an electro-stiffness coupling bioreactor using a lithography-based fabrication methodology and a finite-element-based multiphysics design strategy. Compared to previous EF stimulation devices that have been systematically introduced and classified in Sect. 1, our electro-stiffness bioreactor balances the convenience and robustness of device fabrication, ensures that EFs applied to cells are uniform and can be precisely controlled (Fig. S14 in the supplementary information), and enables us to orthogonally adjust EF strength and the mechanical stiffness across the physiological spectrum.

With the aid of our electro-stiffness coupling bioreactor, we provided an initial framework for the synergistic effect between mechanical and electrical stimulation, from which future studies can be built. Results revealed that matrix stiffness can regulate cellular susceptibility to EFs and exhibited a synergistic role in promoting cancer cell polarization and directional migration, implying that electrical stimulation and mechanical stimulation share interrelated/interacting signal transduction pathways, consistent with previous reports that mechanosensitive Piezo1 channels [45], PI3K [1, 37, 67, 91, 92], and Rho-mediated mechanotransduction pathways [37] can all serve as key modulators for EF-induced cell migration. For example, inhibiting the PI3K pathway has been reported to abolish the electrotaxis of individual cells and cell layers [1, 37, 67, 91, 92]. Mechanosensitive Piezo1 channels were recently reported to be activated by EFs, which induce the extracellular Ca^{2+} influx and further modulate the downstream eNOS/NO pathway [45]. Consistent with the phase diagrams of cellular migration parameters (FMI, velocity, and β index) under different combinations of EFs and stiffness stimulations, which we plotted based on our bioreactor, cancer cells

require a stiffness threshold to respond to EFs, further confirming that reciprocal cellular cross-talk occurs between mechanical and electrical perceptions.

This study also revealed the bidirectional role of the cytoskeleton in the electromechanically triggered cellular polarization and migration. On one hand, results showed that pharmacological inhibition or stabilization of the cytoskeleton (e.g., microfilaments and microtubules) modulated the directional migration of cancer cells induced by electro-stiffness factors, implying that electro-stiffness coupling signals mediate cancer cell migration through cytoskeleton-related mechanisms. Li et al. [93] supported our observation, as EFs were shown to induce the directional migration of neuronal stem/progenitor cells through an *N*-methyl-D-aspartate receptor (NMDAR)/Rac1/actin complex-mediated transduction pathway. This study also emphasized that for cancer cells, the regulatory effect of cytoskeletal dynamics on cellular migration directionality and velocity is consistent, although these two parameters exhibit different sensitivities to cytoskeletal dynamics. On the other hand, this study showed that the electro-stiffness coupling signals can conversely serve as important regulators for the cytoskeleton. The induction of cytoskeleton deformation is highly involved in a series of essential cellular activities, including receptor activation and intracellular signal transduction [94]. EF-stimulated F-actin polarization was recently reported to be triggered by the activation of heparin-binding epidermal growth factor-like growth factor/epidermal growth factor receptor (HB-EGF/EGFR) signaling in keratinocytes [67]. EFs were also reported to excite the contraction of the cytoskeleton, which further induced calcium influx and directed the proangiogenic activities of endothelial cells [45]. The cytoskeleton was reported to alter the adhesion of mesenchymal stem cells (MSCs) through cytoskeleton deformation, which helped MSCs adapt to EF interference and promoted MSC osteogenesis [46]. Building upon these previous studies, we further reported a unique anteroposterior polarization state of the cytoskeleton, in which the cellular head and tail exhibited extremely significant differences under electro-stiffness coupling signals. Specifically, the anterior part of the cancer cell protruded plate-like pseudopodia under electro-stiffness stimulation, whereas the pseudopodia hardly protruded from the posterior part of the cancer cell, which mainly presented an arc-shaped state. That is, the introduction of stiffness information shaped the EF-induced cytoskeleton into a special polarization state, emphasizing the importance of considering the combined effects of electrical and mechanical signals.

Although numerous studies have revealed biochemical mechanisms involved in cancer progression, the comprehensive contributions of biochemical-electro-stiffness coupling signals must be considered. TGF-β1 is a core element of the TME that regulates multiple aspects of cancer cells, including adhesion, migration, cell cycle progression, and apoptosis [88]. The epithelial characteristics of cancer cells are attenuated in response to TGF-β1, which increases the migration and invasion characteristics of cancer cells [95]. Wells and Discher [96] and Pang et al. [97] discussed the cross-talk between biochemical and stiffness cues and confirmed that stiffness promoted the activation of latent TGF-β1. To date, despite a large amount of literature on biochemical and mechanical signals, there is a scarcity of research on the combined effects of electrical and biochemical signals on cellular behaviors, let alone the biochemical electro-stiffness composite signals. A recent study showed that TGF-β1 treatment could enhance fibroblast susceptibility to EFs [98]. Regarding the cross-talk between EF and other biochemical factors, EFs in combination with fibroblast growth factor-2 (FGF-2) reversed the inhibitory effects of FGF-2 on collagen synthesis, and EFs intensified the stimulatory effects of insulin-like growth factor-I on aggrecan synthesis [99]. Compared to previous research, this study pioneered a biochemical–electromechanical microenvironment for cancer cells, in which each parameter can be independently and precisely applied. Moreover, results showed that, in contrast to the cytoskeleton, with a consistent regulatory effect on the directionality and velocity of electromechanical-mediated cancer cell migration, TGF-β1 exerts opposite effects on them. The effect of TGF-β1 on electromechanical-guided cancer cell migration can be amplified by stiffness. Results demonstrated that directionality and velocity were two independent parameters for cancer cell migration under electro-stiffness coupling stimulation, demonstrating the promise of our electro-stiffness bioreactor for applications in biophysical-based cell manipulation.

In summary, we designed and fabricated an electro-stiffness coupling bioreactor that could orthogonally and robustly control the electromechanical coupling stimulations applied to cells without using macroscopic electrodes or salt bridges. Using the bioreactor, we revealed the regulatory role of stiffness on cancer cell susceptibility to EFs, reported the bidirectional modulatory effect of the cytoskeleton on electromechanically mediated cancer cell polarization and migration, and revealed the ability of TGF-β1 to disentangle the directionality and velocity of the electromechanically induced migration of cancer cells. Overall, this study provided a robust and controllable device for the real-time detection and characterization of cellular responses to multicoupled stimuli that contain EFs and stiffness signals. This study elucidated the biophysical mechanisms of cancer cell polarization and migration from the perspective of electro-stiffness coupling and laid a promising foundation for developing novel biophysical methods for cell manipulation and therapeutic interventions involved in cancer invasion and metastasis.

4 Materials and methods

4.1 Electrobioreactor fabrication

We developed the electromechanical coupling bioreactor based on lithography and wet-etching technology (Figs. 1a and 1b; Sect. S1 in the supplementary information). First, ITO glasses were spin-coated with the SUN-9i (Suntific Materials, China) photoresist solution, which was exposed to UV light and treated with the ITO etching solution to fabricate the interdigital microelectrode array. Second, the PI photoresist, with excellent electrical insulation properties, was spin-coated on the ITO surface to isolate the cell culture medium and ITO electrodes in the target region. Third, ITO glasses with patterned electrodes were amino-silanated with 3-aminopropyltrimethoxysilane (Sigma-Aldrich, USA) and glutaraldehyde (Sigma-Aldrich) to create covalent bonds between the ITO chips and PAAm hydrogel layers (Sect. S1 in the supplementary information). We designed and fabricated a PCB to facilitate the connections between the ITO electrodes and the function generator. The completed electrobioreactor is shown in Fig. 1a and Fig. S1 (supplementary information).

4.2 Preparation and functionalization of the physiological stiffness hydrogel layer

In the experiments, the PAAm hydrogel was selected to fabricate a physiological stiffness substrate for cell electrotaxis assays. PAAm hydrogels with the designed mechanical properties were prepared by polymerization of the pre-gel solution containing the desired concentrations of monomer and cross-linker [62, 100]. The PAAm pre-gel solutions containing different ratios of AM (Sigma-Aldrich) to MBA (Sigma-Aldrich) were used to prepare hydrogel layers with specific Young's modulus (1.6 kPa (5% AM–0.15% MBA), 6.8 kPa (10% AM–0.10% MBA), 24.8 kPa (8% AM–0.26% MBA), and 47.9 kPa (10% AM–0.30% MBA)) (Table S1 in the supplementary information). The pre-gel solution was triggered to polymerize by adding 0.1% (volume fraction) N,N,N′,N′-tetramethylethylene diamine (Macklin, China) and 1% (volume fraction) 0.1 g/mL ammonium persulfate (Sigma-Aldrich). The prepared PAAm hydrogels were immersed in complete RPMI 1640 (Gibco, USA) culture medium overnight to remove the unpolymerized monomer.

To facilitate cell adhesion, ECM proteins were covalently bonded to the upper surfaces of PAAm hydrogel layers via the heterobifunctional protein cross-linker sulfosuccinimidyl 6-(4'-azido-2'-nitrophenylamino)hexanoate (sulfo-SANPAH; Thermo Fisher Scientific, USA). In brief, the hydrogel layers were thoroughly rinsed with N-2-hydroxyethylpiperazine-N-2-ethane sulfonic acid (HEPES) (pH 8.5, 50 mmol/L) and coated with a 300-μL sulfo-SANPAH (Thermo Fisher Scientific) at 1.5 mg/mL, which was followed by irradiation with 365 nm UV for 10 min to activate the functional groups. Next, PAAm layers were thoroughly rinsed with HEPES to remove the unreacted sulfo-SANPAH. Finally, the gel samples were functionalized by fibronectin (Sigma-Aldrich) by incubating the fibronectin solution on the hydrogel layers at 20 μg/mL overnight at 4 °C (Sect. S2 in the supplementary information).

4.3 Stiffness characterization based on nanoindentation

A nanoindenter (Chiaro, Piuma) was employed to quantify the stiffness of the PAAm layer in our electro-stiffness bioreactor. Before detection, the hydrogels were fully swollen in RPMI 1640 complete medium for 24 h. The indentation probe suitable for measuring the hydrogel materials was used. The spring constant (k) of the indentation probe was 0.500 N/m, with a spherical indentation tip whose radius was 26,000 μm. For all nanoindentation tests, the loading rate was set as 5.0 μm/s, with a loading duration of 2 s.

4.4 Finite-element simulation for characterizing the spatial distributions of EFs

EFs generated by the ITO microelectrode array penetrated the PAAm hydrogel layer and were distributed in the chip chamber (Figs. 1d and 1e). According to the geometrical and position parameters of EF-related elements of the bioreactor, a finite-element model was established, which mainly consisted of a pair of ITO electrodes, a PAAm hydrogel layer, and a cell culture medium (Figs. 1c and 1d). Free triangular meshes were selected to divide the geometric model, and further mesh optimization was carried out for the electric signal-induced region (Fig. S6a in the supplementary information). The meshing results of the geometric model showed that there were approximately 1,000,000 triangular elements. The electrical parameters (i.e., conductivity and dielectric constant) of EF-related materials of the bioreactor were measured using an electrochemical workstation (CHI 760 E, CH Instruments, Inc., USA) (Sect. S3 in the supplementary information). The parameters of the material properties involved in the simulation analysis are listed in Table S2 (supplementary information), and the simulation results are displayed in Figs. 1d and 1e and Fig. S6 (supplementary information).

4.5 Cell culture

The human nonsmall cell lung carcinoma cell line A549 (ATCC) was maintained in RPMI 1640 culture medium supplemented with 10% fetal bovine serum (Gibco) and 100 U/mL penicillin/streptomycin (Gibco) at 37 °C in a

humidified 5% CO_2 incubator. A549 cells were harvested and subcultured with 0.25% trypsin (Gibco) when they reached 85% confluence, and cells were seeded in an electro-stiffness-coupled bioreactor at a density of approximately 5×10^4 cells/chip.

4.6 Image acquisition and data processing

In the experiments, A549 cells were first seeded on the upper surface of the functionalized PAAm hydrogel layer of the electro-stiffness coupling bioreactor. The bioreactor was placed into the culture chamber of a Nikon (Tokyo, Japan) live-cell workstation. Cell trajectories were imaged every 5 min for a total duration of 3 h via a built-in Nikon microscope (20× objective lens), and images were analyzed using ImageJ (1.51v). At least 50 cells were randomly selected for each sample group unless otherwise stated. Cells undergoing division, death, or migration outside the field of view were excluded from the analysis. For the cell viability assay, cells were treated with a live/dead staining solution (Thermo Fisher Scientific) containing 2 μmol/L calcein-AM and 4 μmol/L EthD-1, which were dissolved in Dulbecco's phosphate-buffered saline (DPBS) (Gibco) for 30 min, and washed thoroughly with DPBS (Gibco) thrice. The fluorescence images of the stained cells were obtained using a spinning disk confocal system (UltraView VOX, PerkinElmer, USA).

4.7 Definitions of cell migration indices

To quantify cell locomotion under electro-stiffness coupling conditions, several migration indices were defined based on the established Cartesian coordinate system (Fig. 2c), i.e., FMI, migration velocity (V), MSD, and β index. In the Cartesian coordinate system, the starting point of each single cell was set as (0, 0), and cell migration trajectories were recorded via a series of coordinate positions (Fig. 2c). For computational convenience, the positive direction of the Y-axis was set to be parallel to EFID. FMI, which is the directionality of cellular migration parallel ($FMI^{//}_{EF}$) or perpendicular ($FMI^{\perp}_{EF}$) to EFID, was calculated using the following equations [23, 48]:

$$FMI^{//}_{EF} = \frac{1}{m}\sum\frac{y_{end}}{d_{accum}}, \tag{1a}$$

$$FMI^{\perp}_{EF} = \frac{1}{m}\sum\frac{x_{end}}{d_{accum}}, \tag{1b}$$

where (x_{end}, y_{end}) and d_{accum} are the end point and total length of a single-cell trajectory respectively, and m is the total number of tracked cells. The superscripts $\perp$ or // represent the reference direction of FMI, which was perpendicular or parallel to EFID, respectively (Fig. 2c). According to the definitions of FMI, $FMI^{//}_{EF}=1$ or -1 indicated that cells migrate along or against the EFID, respectively; $FMI^{//}_{EF}=0$ indicated that cells did not exhibit directional migration parallel to EFID.

Cell migration velocity (V) was defined as the ratio of the accumulated distance to the induction time, which can be expressed as follows [101]:

$$V=\frac{\sqrt{(x_i-x_{i-1})^2+(y_i-y_{i-1})^2}}{T}, \tag{2}$$

where (x_i, y_i) is the coordinate position at the ith time point, and T is the total induction time.

The MSD index refers to the mean squared distance between two corresponding positions at time $t(i\times(n\times\Delta t))$ and $t((i+1)\times(n\times\Delta t))$, which can be expressed as follows [101, 102]:

$$\begin{aligned}\left\langle d^2(t)\right\rangle &= \mathrm{MSD}(n\times\Delta t)\\ &= \frac{1}{N-n}\sum_{i=1}^{N-n}\left[(x_{i+n}-x_i)^2+(y_{i+n}-y_i)^2\right],\end{aligned} \tag{3}$$

where (x_{i+n}, y_{i+n}) is the coordinate position at the ($i+n$)th time point, n and N are the time step number and the total number of frames respectively, Δt=5 min is the time interval between two adjacent frames, and $n\times\Delta t$ is the time interval between the combined trajectories (n=1, 2, ⋯, 36). The growth of MSD over time complied with a power-law relationship, which can be expressed as follows [101, 102]:

$$\mathrm{MSD}(t)\approx t^{\beta(t)}, \tag{4}$$

where β is a measurement of cell migration persistence.

4.8 Definitions of cell shape factors

Shape factors were adopted for the quantitative characterization of cell polarization morphologies, i.e., the spreading area, circularity (Circ), and aspect ratio (AR). Circ can be calculated by the following equation:

$$\mathrm{Circ}=\frac{4\times\pi\times A}{C^2}, \tag{5}$$

where A and C denote the spreading area and perimeter of cells, respectively. Hence, Circ∈[0, 1]. Circ=1 is a perfect circle, whereas Circ→0 implies a gradually elongated polygon. The contour of each cell can be extracted and fitted as an ellipse using ImageJ. Hence, the AR index can be expressed as follows:

$$\mathrm{AR}=\frac{L_{(\mathrm{major\ axis})}}{L_{(\mathrm{minor\ axis})}}, \tag{6}$$

where $L_{(\mathrm{major\ axis})}$ and $L_{(\mathrm{minor\ axis})}$ denote the lengths of the major and minor axes of the ellipse fitted to the cell boundary, respectively.

4.9 Drug treatments

CytoD (Abcam, UK) was used as an inhibitor of microfilaments at 0.01, 0.1, 0.5, and 1.0 μmol/L. Jasp (Abcam, UK) was used as the stabilizer of microfilaments at 0.01, 0.05, 0.1, and 0.2 μmol/L. CytoD and Jasp were predissolved in dimethyl sulfoxide (DMSO) to generate a 1.0-mmol/L stock solution. COL (Sigma-Aldrich) was used as an inhibitor of microtubules at 0.1, 1, 5, and 10 μmol/L. EpoD (Sigma-Aldrich) was used as a microtubule stabilizer at 1, 10, 50, and 100 nmol/L. COL and EpoD were predissolved in DMSO to generate 10 mmol/L stock solutions.

For TGF-β1 treatment, recombinant human TGF-β1 protein (R&D Systems, USA) was predissolved at 20 μg/mL in a sterile 4 mmol/L HCl solution containing 1 mg/mL bovine serum albumin (BSA) and stored at 20 °C. After passage, a complete culture medium was added to A549 cells, which were cultured in an incubator for 2 h. After cells were fully spread on the substrate, the complete culture medium was removed, and cells were treated with 0.5, 1, 2, or 5 ng/mL TGF-β1 for 48 h.

4.10 Immunofluorescence staining

Cells were first fixed with 4% (0.04 g/mL) paraformaldehyde solution (Yuanye Bio-Technology, China) for 30 min at 4 °C. The fixed cells were permeabilized with 0.2% (volume fraction) Triton X-100 (Sigma-Aldrich) in DPBS for 5 min, followed by blocking with a 5% (0.05 g/mL) BSA (Sigma-Aldrich) solution for 30 min at room temperature. For vinculin staining, cells were incubated with a monoclonal anti-vinculin antibody (Abcam) diluted 1: 100 in 1% BSA overnight at 4 °C and incubated with the corresponding fluorescein isothiocyanate (FITC)-labeled secondary antibody (Abcam) diluted 1:100 overnight at 4 °C. Actin microfilaments were stained with 100 nmol/L tetramethylrhodamine isothiocyanate (TRITC)-labeled phalloidin (Yeasen, China) overnight at 4 °C. Nuclei were stained with 4',6-diamidino-2-phenylindole (DAPI; Yuanye Bio-Technology) at 5 μg/mL for 30 min at room temperature.

4.11 Statistical analysis

For all assays presented as bar chart, data are expressed as mean±standard deviation. For all assays presented as line chart, data are expressed as mean±standard error of the mean. For all assays presented as box chart, the box expresses the maximum, minimum, median, and upper and lower quartiles of a set of data, unless otherwise noted. Statistical analyses were performed using one-way analysis of variance (ANOVA), followed by Student's *t*-test using GraphPad Prism. Significant differences were denoted as $^{*}P<0.05$, $^{**}P<0.01$, $^{***}P<0.001$, and $^{****}P<0.0001$.

Supplementary Information The online version contains supplementary material available at https://doi.org/10.1631/bdm.2400280.

Acknowledgements We thank Prof. Chunyang Xiong (College of Engineering, Peking University) and Prof. Jianyong Huang (College of Engineering, Peking University) for their assistance with confocal imaging, as well as their helpful suggestions and discussions regarding this project. Beijing Academy of Science and Technology (BJAST) supported this work. This work was supported by the Financial Program of BJAST (Nos. 24CE-BGS-02, 24CA010-01, and 23CB106).

Author contributions QZ and QFY jointly completed the experiment and data collection. QFY contributed to the bioreactor design and finite-element simulation. QZ contributed to the data analysis and manuscript writing. Both authors reviewed the manuscript.

Declarations

Conflict of interest The authors declare that they have no conflict of interest.

Ethical approval The human cancer cell line A549 used in this study was obtained from American Type Culture Collection (ATCC). No primary human/animal tissues were involved in this study.

Data availability The data that support the findings of this study are available from the corresponding author upon reasonable request.

References

1. SenGupta S, Parent CA, Bear JE (2021) The principles of directed cell migration. Nat Rev Mol Cell Biol 22(8):529–547. https://doi.org/10.1038/s41580-021-00366-6
2. Yun J, Jin X, Sun Q et al (2022) Transcriptional analysis of mice melanoma B16-F10 cells in response to directed current electric fields. Bioelectromagnetics 43(5):297–308. https://doi.org/10.1002/bem.22412
3. Fontani V, Cruciani S, Santaniello S et al (2023) Impact of REAC regenerative endogenous bioelectrical cell reprogramming on MCF7 breast cancer cells. J Pers Med 13(6):1019. https://doi.org/10.3390/jpm13061019
4. McCaig CD, Rajnicek AM, Song B et al (2005) Controlling cell behavior electrically: current views and future potential. Physiol Rev 85(3):943–978. https://doi.org/10.1152/physrev.00020.2004
5. Lange F, Porath K, Sellmann T et al (2023) Direct-current electrical field stimulation of patient-derived colorectal cancer cells. Biology 12(7):1032. https://doi.org/10.3390/biology12071032
6. Levin M (2021) Bioelectric signaling: reprogrammable circuits underlying embryogenesis, regeneration, and cancer. Cell 184(8): 1971–1989. https://doi.org/10.1016/j.cell.2021.02.034
7. Sun YS (2017) Studying electrotaxis in microfluidic devices. Sensors 17(9):2048. https://doi.org/10.3390/s17092048
8. Sun YS, Peng SW, Cheng JY (2012) In vitro electrical-stimulated wound-healing chip for studying electric field-assisted wound-healing process. Biomicrofluidics 6(3):34117. https://doi.org/10.1063/1.4750486
9. McCaig CD, Song B, Rajnicek AM (2009) Electrical dimensions

in cell science. J Cell Sci 122(Pt 23):4267–4276. https://doi.org/10.1242/jcs.023564
10. Wu SY, Hou HS, Sun YS et al (2015) Correlation between cell migration and reactive oxygen species under electric field stimulation. Biomicrofluidics 9(5):054120. https://doi.org/10.1063/1.4932662
11. Thompson JA, Kashon ML, McKinney W et al (2024) High-fat Western diet alters crystalline silica-induced airway epithelium ion transport but not airway smooth muscle reactivity. BMC Res Notes 17(1):13. https://doi.org/10.1186/s13104-023-06672-w
12. Ivanova R, Benton DCH, Munye MM et al (2019) A nanosensor toolbox for rapid, label-free measurement of airway surface liquid and epithelial cell function. ACS Appl Mater Interfaces 11(9):8731–8739. https://doi.org/10.1021/acsami.8b14122
13. da Cunha MF, Simonin J, Sassi A et al (2016) Analysis of nasal potential in murine cystic fibrosis models. Int J Biochem Cell Biol 80:87–97. https://doi.org/10.1016/j.biocel.2016.10.001
14. Lazrak A, Jurkuvenaite A, Ness EC et al (2014) Inter-α-inhibitor blocks epithelial sodium channel activation and decreases nasal potential differences in ΔF508 mice. Am J Respir Cell Mol Biol 50(5):953–962. https://doi.org/10.1165/rcmb.2013-0215OC
15. Maouche K, Medjber K, Zahm JM et al (2013) Contribution of α7 nicotinic receptor to airway epithelium dysfunction under nicotine exposure. Proc Natl Acad Sci USA 110(10):4099–4104. https://doi.org/10.1073/pnas.1216939110
16. Gerbino A, Debellis L, Caroppo R et al (2010) Cadmium inhibits acid secretion in stimulated frog gastric mucosa. Toxicol Appl Pharmacol 245(2):264–271. https://doi.org/10.1016/j.taap.2010.03.010
17. Teixeira MA, Chaguri L, Carissimi AS et al (2006) Effects of an individually ventilated cage system on the airway integrity of rats (*Rattus norvegicus*) in a laboratory in Brazil. Lab Anim 40(4): 419–431. https://doi.org/10.1258/002367706778476398
18. Nakagawa NK, Donato-Júnior F, Kondo CS et al (2004) Effects of acute hypovolaemia by furosemide on tracheal transepithelial potential difference and mucus in dogs. Eur Respir J 24(5): 805–810. https://doi.org/10.1183/09031936.04.10021704
19. Egli M, Duplain H, Lepori M et al (2004) Defective respiratory amiloride-sensitive sodium transport predisposes to pulmonary oedema and delays its resolution in mice. J Physiol 560(Pt 3): 857–865. https://doi.org/10.1113/jphysiol.2004.066704
20. Kanoh S, Tamaoki J, Kondo M et al (2001) Effects of new quinolones on transepithelial electrical potential difference of tracheal mucosa in vivo. Antimicrob Agents Chemother 45(10): 2928–2930. https://doi.org/10.1128/AAC.45.10.2928-2930.2001
21. Hatzoglou CH, Gourgoulianis KI, Molyvdas PA (2001) Effects of SNP, ouabain, and amiloride on electrical potential profile of isolated sheep pleura. J Appl Physiol 90(4):1565–1569. https://doi.org/10.1152/jappl.2001.90.4.1565
22. Hebestreit A, Kersting U, Basler B et al (2001) Exercise inhibits epithelial sodium channels in patients with cystic fibrosis. Am J Respir Crit Care Med 164(3):443–446. https://doi.org/10.1164/ajrccm.164.3.2007168
23. Kim MS, Lee MH, Kwon BJ et al (2014) Effects of direct current electric-field using ITO plate on breast cancer cell migration. Biomater Res 18(1):10. https://doi.org/10.1186/2055-7124-18-10
24. Liu ZR, Wan XY, Wang ZL et al (2021) Electroactive biomaterials and systems for cell fate determination and tissue regeneration: design and applications. Adv Mater 33(32):e2007429. https://doi.org/10.1002/adma.202007429
25. Guillot-Ferriols M, Lanceros-Méndez S, Ribelles JLG et al (2022) Electrical stimulation: effective cue to direct osteogenic differentiation of mesenchymal stem cells? Biomater Adv 138: 212918. https://doi.org/10.1016/j.bioadv.2022.212918
26. Xiang XW, Liu HT, Liu W et al (2023) Revolutionizing wound healing: ultrashort pulse electric fields in seconds for highly aligned extracellular matrix and efficient cell migration. Chem Eng J 471:144267. https://doi.org/10.1016/j.cej.2023.144267
27. MacCarthy-Morrogh L, Martin P (2020) The hallmarks of cancer are also the hallmarks of wound healing. Sci Signal 13(648): eaay8690. https://doi.org/10.1126/scisignal.aay8690
28. Zhao HR, Zhang WJ, Tang XW et al (2023) Electrostatic potential difference between tumor and paratumor regulates cancer stem cell behavior and prognose tumor spread. Bioeng Transl Med 8(2):e10399. https://doi.org/10.1002/btm2.10399
29. Zhu K, Hum NR, Reid B et al (2020) Electric fields at breast cancer and cancer cell collective galvanotaxis. Sci Rep 10(1): 8712. https://doi.org/10.1038/s41598-020-65566-0
30. Murugan NJ, Cariba S, Abeygunawardena S et al (2024) Biophysical control of plasticity and patterning in regeneration and cancer. Cell Mol Life Sci 81(1):9. https://doi.org/10.1007/s00018-023-05054-6
31. Sheth M, Esfandiari L (2022) Bioelectric dysregulation in cancer initiation, promotion, and progression. Front Oncol 12: 846917. https://doi.org/10.3389/fonc.2022.846917
32. Huynh PK, Nguyen D, Binder G et al (2023) Multifractality in surface potential for cancer diagnosis. J Phys Chem B 127(31): 6867–6877. https://doi.org/10.1021/acs.jpcb.3c01733
33. Li XF, Kolega J (2022) Effects of direct current electric fields on cell migration and actin filament distribution in bovine vascular endothelial cells. J Vasc Res 39(5):391–404. https://doi.org/10.1159/000064517
34. Cuzick J, Holland R, Barth V et al (1998) Electropotential measurements as a new diagnostic modality for breast cancer. Lancet 352(9125):359–363. https://doi.org/10.1016/s0140-6736(97)10002-2
35. Tian JS, Tay A (2023) Progress on electro-enhancement of cell manufacturing. Small Methods 8(7):e2301281. https://doi.org/10.1002/smtd.202301281
36. Yao L, Tran K, Nguyen D (2022) Collagen matrices mediate glioma cell migration induced by an electrical signal. Gels 8(9): 545. https://doi.org/10.3390/gels8090545
37. Yao L, Shanley L, McCaig C et al (2008) Small applied electric

fields guide migration of hippocampal neurons. J Cell Physiol 216(2):527–535. https://doi.org/10.1002/jcp.21431
38. Cho Y, Son M, Jeong H et al (2018) Electric field-induced migration and intercellular stress alignment in a collective epithelial monolayer. Mol Biol Cell 29(19):2292–2302. https://doi.org/10.1091/mbc.E18-01-0077
39. Xiong GM, Do AT, Wang JK et al (2015) Development of a miniaturized stimulation device for electrical stimulation of cells. J Biol Eng 9:14. https://doi.org/10.1186/s13036-015-0012-1
40. Li YP, Xu T, Zou H et al (2017) Cell migration microfluidics for electrotaxis-based heterogeneity study of lung cancer cells. Biosens Bioelectron 89(Pt 2):837–845. https://doi.org/10.1016/j.bios.2016.10.002
41. Chou TY, Sun YS, Hou HS et al (2016) Designing microfluidic devices for studying cellular responses under single or coexisting chemical/electrical/shear stress stimuli. J Vis Exp 114:54397. https://doi.org/10.3791/54397
42. Lo KY, Wu SY, Sun YS (2016) A microfluidic device for studying the production of reactive oxygen species and the migration in lung cancer cells under single or coexisting chemical/electrical stimulation. Microfluid Nanofluid 20(1):15. https://doi.org/10.1007/s10404-015-1683-0
43. Halldorsson S, Lucumi E, Gómez-Sjöberg R et al (2015) Advantages and challenges of microfluidic cell culture in polydimethylsiloxane devices. Biosens Bioelectron 63:218–231. https://doi.org/10.1016/j.bios.2014.07.029
44. Leal J, Shaner S, Jedrusik N et al (2023) Electrotaxis evokes directional separation of co-cultured keratinocytes and fibroblasts. Sci Rep 13(1):11444. https://doi.org/10.1038/s41598-023-38664-y
45. Li CH, Yu P, Wang ZG et al (2023) Electro-mechanical coupling directs endothelial activities through intracellular calcium ion deployment. Mater Horiz 10(11):4903–4913. https://doi.org/10.1039/d3mh01049j
46. Chen ST, He SY, Li Y et al (2023) Metallurgical manipulation of surface Volta potential in bimetals and cell response of human mesenchymal stem cells. Biomater Adv 153:213529. https://doi.org/10.1016/j.bioadv.2023.213529
47. Kim MS, Lee MH, Kwon BJ et al (2017) Control of neonatal human dermal fibroblast migration on poly(lactic-co-glycolic acid)-coated surfaces by electrotaxis. J Tissue Eng Regen Med 11(3):862–868. https://doi.org/10.1002/term.1986
48. Kim MS, Lee MH, Kwon BJ et al (2015) Golgi polarization plays a role in the directional migration of neonatal dermal fibroblasts induced by the direct current electric fields. Biochem Biophys Res Commun 460(2):255–260. https://doi.org/10.1016/j.bbrc.2015.03.021
49. Tsai HF, Ijspeert C, Shen AQ (2020) Voltage-gated ion channels mediate the electrotaxis of glioblastoma cells in a hybrid PMMA/PDMS microdevice. APL Bioeng 4(3):036102. https://doi.org/10.1063/5.0004893
50. Thrivikraman G, Boda SK, Basu B (2018) Unraveling the mechanistic effects of electric field stimulation towards directing stem cell fate and function: a tissue engineering perspective. Biomaterials 150:60–86. https://doi.org/10.1016/j.biomaterials.2017.10.003
51. Zajdel TJ, Shim G, Wang L et al (2020) SCHEEPDOG: programming electric cues to dynamically herd large-scale cell migration. Cell Syst 10(6):506–514. https://doi.org/10.1016/j.cels.2020.05.009
52. Abasi S, Aggas JR, Venkatesh N et al (2020) Design, fabrication and testing of an electrical cell stimulation and recording apparatus (ECSARA) for cells in electroculture. Biosens Bioelectron 147:111793. https://doi.org/10.1016/j.bios.2019.111793
53. Kim HN, Kang DH, Kim MS et al (2012) Patterning methods for polymers in cell and tissue engineering. Ann Biomed Eng 40(6):1339–1355. https://doi.org/10.1007/s10439-012-0510-y
54. Janmey PA, Fletcher DA, Reinhart-King CA (2020) Stiffness sensing by cells. Physiol Rev 100(2):695–724. https://doi.org/10.1152/physrev.00013.2019
55. Saraswathibhatla A, Indana D, Chaudhuri O (2023) Cell–extracellular matrix mechanotransduction in 3D. Nat Rev Mol Cell Biol 24(7):495–516. https://doi.org/10.1038/s41580-023-00583-1
56. Bavi N, Richardson J, Heu C et al (2019) PIEZO1-mediated currents are modulated by substrate mechanics. ACS Nano 13(11):13545–13559. https://doi.org/10.1021/acsnano.9b07499
57. Ladoux B, Mege RM (2017) Mechanobiology of collective cell behaviours. Nat Rev Mol Cell Biol 18(12):743–757. https://doi.org/10.1038/nrm.2017.98
58. Gilkes DM, Semenza GL, Wirtz D (2014) Hypoxia and the extracellular matrix: drivers of tumour metastasis. Nat Rev Cancer 14(6):430–439. https://doi.org/10.1038/nrc3726
59. Yuan ZN, Li YP, Zhang SF et al (2023) Extracellular matrix remodeling in tumor progression and immune escape: from mechanisms to treatments. Mol Cancer 22(1):48. https://doi.org/10.1186/s12943-023-01744-8
60. Nia HT, Munn LL, Jain RK (2020) Physical traits of cancer. Science 370(6516):eaaz0868. https://doi.org/10.1126/science.aaz0868
61. Velez DO, Tsui B, Goshia T et al (2017) 3D collagen architecture induces a conserved migratory and transcriptional response linked to vasculogenic mimicry. Nat Commun 8(1):1651. https://doi.org/10.1038/s41467-017-01556-7
62. Tse JR, Engler AJ (2010) Preparation of hydrogel substrates with tunable mechanical properties. Curr Protoc Cell Biol 47(1):10.16.1–10.16.16. https://doi.org/10.1002/0471143030.cb1016s47
63. Wang K, Shi L, Linthicum W et al (2019) Substrate stiffness-dependent carbon nanotube-induced lung fibrogenesis. Nano Lett 19(8):5443–5451. https://doi.org/10.1021/acs.nanolett.9b01943
64. Marinelli JP, Levin DL, Vassallo R et al (2017) Quantitative assessment of lung stiffness in patients with interstitial lung disease using MR elastography. J Magn Reson Imaging 46(2):365–374. https://doi.org/10.1002/jmri.25579
65. Miyazawa A, Ito S, Asano S et al (2018) Mechanobiology of lung cancer cells: regulation of PD-L1 expression by matrix stiffness. J Thorac Oncol 13(10):S518. https://doi.org/10.1016/j.jtho.2018.08.699
66. Miyazawa A, Ito S, Asano S et al (2018) Regulation of PD-L1 expression by matrix stiffness in lung cancer cells. Biochem

Biophys Res Commun 495(3):2344–2349. https://doi.org/10.1016/j.bbrc.2017.12.115
67. Liu XQ, Yang JR, Kong M et al (2023) CD9 negatively regulates collective electrotaxis of the epidermal monolayer by controlling and coordinating the polarization of leader cells. Burns Trauma 11:tkad012. https://doi.org/10.1093/burnst/tkad012
68. Mayor R, Etienne-Manneville S (2016) The front and rear of collective cell migration. Nat Rev Mol Cell Biol 17(2):97–109. https://doi.org/10.1038/nrm.2015.14
69. Takanezawa Y, Nakamura R, Sone Y et al (2017) Variation in the activity of distinct cytochalasins as autophagy inhibitiors in human lung A549 cells. Biochem Biophys Res Commun 494(3–4):641–647. https://doi.org/10.1016/j.bbrc.2017.10.135
70. Luo YF, Zhang M, Dai JG et al (2016) Cytochalasins from mangrove endophytic fungi *Phomopsis* spp. xy21 and xy22. Phytochem Lett 17:162–166. https://doi.org/10.1016/j.phytol.2016.07.027
71. Burns JL, Jonas M, Chi EY et al (1996) Invasion of respiratory epithelial cells by *Burkholderia* (*Pseudomonas*) *cepacia*. Infect Immun 64(10):4054–4059. https://doi.org/10.1128/iai.64.10.4054-4059.1996
72. Tu LN, Jeong HY, Kwon HY et al (2007) Modulation of adherence, invasion, and tumor necrosis factor alpha secretion during the early stages of infection by *Streptococcus pneumoniae* ClpL. Infect Immun 75(6):2996–3005. https://doi.org/10.1128/IAI.01716-06
73. Hayot C, Debeir O, Van Ham P et al (2006) Characterization of the activities of actin-affecting drugs on tumor cell migration. Toxicol Appl Pharmacol 211(1):30–40. https://doi.org/10.1016/j.taap.2005.06.006
74. Schwingshackl A, Roan E, Teng B et al (2015) TREK-1 regulates cytokine secretion from cultured human alveolar epithelial cells independently of cytoskeletal rearrangements. PloS One 10(5):e0126781. https://doi.org/10.1371/journal.pone.0126781
75. Sargsyan A, Sahakyan H, Nazaryan K (2023) Effect of colchicine binding site inhibitors on the tubulin intersubunit interaction. ACS Omega 8(32):29448–29454. https://doi.org/10.1021/acsomega.3c02979
76. Wang JX, Miller DD, Li W (2022) Molecular interactions at the colchicine binding site in tubulin: an X-ray crystallography perspective. Drug Discov Today 27(3):759–776. https://doi.org/10.1016/j.drudis.2021.12.001
77. Nair RR, Sherry DM, Schwarz LA (2007) Colchicine-mediated focal adhesion formation promotes transient, lipoplex-mediated transfection of A549 cells. Gene Ther Mol Biol 11A:1–13
78. Wasylnka JA, Moore MM (2002) Uptake of *Aspergillus fumigatus* conidia by phagocytic and nonphagocytic cells in vitro: quantitation using strains expressing green fluorescent protein. Infect Immun 70(6):3156–3163. https://doi.org/10.1128/IAI.70.6.3156-3163.2002
79. Jung HI, Shin I, Park YM et al (1997) Colchicine activates actin polymerization by microtubule depolymerization. Mol Cells 7(3):431–437
80. Teng Y, Zhu K, Xiong CY et al (2018) Electrodeformation-based biomechanical chip for quantifying global viscoelasticity of cancer cells regulated by cell cycle. Anal Chem 90(14):8370–8378. https://doi.org/10.1021/acs.analchem.8b00584
81. Fong CHY, Lu L, Chen LL et al (2022) Interferon-gamma inhibits influenza A virus cellular attachment by reducing sialic acid cluster size. iScience 25(4):104037. https://doi.org/10.1016/j.isci.2022.104037
82. Cramer LP (1999) Role of actin-filament disassembly in lamellipodium protrusion in motile cells revealed using the drug jasplakinolide. Curr Biol 9(19):1095–1105. https://doi.org/10.1016/s0960-9822(99)80478-3
83. Brunden KR, Zhang B, Carroll J et al (2010) Epothilone D improves microtubule density, axonal integrity, and cognition in a transgenic mouse model of tauopathy. J Neurosci 30(41):13861–13866. https://doi.org/10.1523/JNEUROSCI.3059-10.2010
84. Andrieux A, Salin P, Schweitzer A et al (2006) Microtubule stabilizer ameliorates synaptic function and behavior in a mouse model for schizophrenia. Biol Psychiatry 60(11):1224–1230. https://doi.org/10.1016/j.biopsych.2006.03.048
85. Clark JA, Chuckowree JA, Dyer MS et al (2020) Epothilone D alters normal growth, viability and microtubule dependent intracellular functions of cortical neurons in vitro. Sci Rep 10(1):918. https://doi.org/10.1038/s41598-020-57718-z
86. Dietzmann A, Kanakis D, Kirches E et al (2003) Nanomolar concentrations of epothilone D inhibit the proliferation of glioma cells and severely affect their tubulin cytoskeleton. J Neurooncol 65(2):99–106. https://doi.org/10.1023/b:neon.0000003679.40609.63
87. Petroni G, Buqué A, Coussens LM et al (2022) Targeting oncogene and non-oncogene addiction to inflame the tumour microenvironment. Nat Rev Drug Discov 21(6):440–462. https://doi.org/10.1038/s41573-022-00415-5
88. Goenka A, Khan F, Verma B et al (2023) Tumor microenvironment signaling and therapeutics in cancer progression. Cancer Commun 43(5):525–561. https://doi.org/10.1002/cac2.12416
89. Leal T, Kotecha R, Ramlau R et al (2023) Tumor treating fields therapy with standard systemic therapy versus standard systemic therapy alone in metastatic non-small-cell lung cancer following progression on or after platinum-based therapy (LUNAR): a randomised, open-label, pivotal phase 3 study. Lancet Oncol 24(9):1002–1017. https://doi.org/10.1016/S1470-2045(23)00344-3
90. Lee WS, Jang Y, Cho A et al (2023) Effectiveness of tumor-treating fields to reduce the proliferation and migration of liposarcoma cell lines. Exp Ther Med 26(2):363. https://doi.org/10.3892/etm.2023.12062
91. Zhao M, Song B, Pu J et al (2006) Electrical signals control wound healing through phosphatidylinositol-3-OH kinase-γ and PTEN. Nature 442(7101):457–460. https://doi.org/10.1038/nature04925
92. Liu Q, Song B (2014) Electric field regulated signaling pathways. Int J Biochem Cell Biol 55:264–268. https://doi.org/10.1016/j.biocel.2014.09.014
93. Li L, El-Hayek YH, Liu BS et al (2008) Direct-current electrical field guides neuronal stem/progenitor cell migration. Stem Cells 26(8):2193–2200. https://doi.org/10.1634/stemcells.2007-1022
94. Seetharaman S, Etienne-Manneville S (2020) Cytoskeletal crosstalk in cell migration. Trends Cell Biol 30(9):720–735. https://doi.org/10.1016/j.tcb.2020.06.004

95. Derynck R, Turley SJ, Akhurst RJ (2021) TGFβ biology in cancer progression and immunotherapy. Nat Rev Clin Oncol 18(1):9–34. https://doi.org/10.1038/s41571-020-0403-1
96. Wells RG, Discher DE (2008) Matrix elasticity, cytoskeletal tension, and TGF-β: the insoluble and soluble meet. Sci Signal 1(10):pe13. https://doi.org/10.1126/stke.110pe13
97. Pang MS, Teng Y, Huang JY et al (2017) Substrate stiffness promotes latent TGF-β1 activation in hepatocellular carcinoma. Biochem Biophys Res Commun 483(1):553–558. https://doi.org/10.1016/j.bbrc.2016.12.107
98. Pavlenko A, Lasota S, Wnuk D et al (2023) Bronchial fibroblasts from asthmatic patients display impaired responsiveness to direct current electric fields (dcEFs). Biomedicines 11(8):2138. https://doi.org/10.3390/biomedicines11082138
99. Kozaci LD, Bilgin MD, Çarhan A et al (2019) Effects of low-frequency electromagnetic fields on chondrocytes in short-term cultures. Cyprus J Med Sci 4(3):201–207. https://doi.org/10.5152/cjms.2019.804
100. Mohammed D, Versaevel M, Bruyere C et al (2019) Innovative tools for mechanobiology: unraveling outside-in and inside-out mechanotransduction. Front Bioeng Biotechnol 7:162. https://doi.org/10.3389/fbioe.2019.00162
101. Xu JM, Chen C, Jiang XM et al (2011) Effects of micropatterned curvature on the motility and mechanical properties of airway smooth muscle cells. Biochem Biophys Res Commun 415(4):591–596. https://doi.org/10.1016/j.bbrc.2011.10.111
102. Dieterich P, Klages R, Preuss R et al (2008) Anomalous dynamics of cell migration. Proc Natl Acad Sci USA 105(2):459–463. https://doi.org/10.1073/pnas.0707603105